International Journal of Plasticity 171 (2023) 103813

Contents lists available at ScienceDirect

International Journal of Plasticity

journal homepage: www.elsevier.com/locate/ijplas

Ductile ultrastrong China low activation martensitic steel with lamellar grain structure

J.H. Zhou [a,*], J. Wang [b], Robert O. Ritchie [c,*], Y.C. Wu [d], J.W. Cheng [e], L. Wang [a], X.W. Yin [a], Y.F. Jiang [a], J.G. Ren [a]

[a] *The Key Laboratory of Reliability and Health Management of Energy and Power Equipment in Liaoning Province, School of Mechanical Engineering, Shenyang Institute of Engineering, Shenyang 110136, China*

[b] *National Engineering Research Center of Light Alloy Net Forming and State Key Laboratory of Metal Matrix Composite, School of Materials Science and Engineering, Shanghai Jiao Tong University, Shanghai 200240, China*

[c] *Department of Materials Science and Engineering, University of California, Berkeley, Berkeley, CA 94720, USA*

[d] *Shenzhen Focalon Applied Academy, Shenzhen Practical Scientific Research Co., Ltd, Shenzhen 518132, China*

[e] *Key Laboratory of Liaoning Advanced Welding and Joining Technology, School of Material Science and Engineering, Dalian University of Technology, Dalian 116024, China*

A R T I C L E I N F O

Keywords:
CLAM steel
Ductility mechanism
Lamellar structure
Delamination cracks
Local stress concentration

A B S T R A C T

The low high-temperature mechanical properties of reduced activated ferrite martensitic (RAFM) heat-resistant steels limit the maximum operating temperature of nuclear fusion reactors. However, it is difficult to improve the strength of the material without reducing its plasticity. In this study we prepared a China low activation martensitic (CLAM) steel with a layered structure through hot rolling followed by low-temperature tempering, which successfully improved its strength and ductility. In addition, we elucidate the ductility mechanisms in such lamellar structural materials. When the strength of the grain boundaries exceeds that of the grains, cracks will continuously extend along the layered grain boundaries, eventually resulting in a delamination fracture mechanism. When the grain strength exceeds that of the grain boundaries, cracks will continuously form through the relative sliding of the grain boundaries, and a large number of small cracks will initiate and propagate longitudinally along the layered boundaries. Both forms of crack propagation cause longitudinal expansion along the layered grain boundaries. The resulting longitudinal extension of cracks markedly diminishes local stress concentration to promote plastic deformation, thereby significantly increasing the ductility of the material. Employing the combination of this delamination ductility mechanism with interface strengthening and precipitation strengthening, the strength of the CLAM steel for nuclear applications is shown to be enhanced by ~30 % without loss of elongation. The current delamination ductility strategy provides a unique pathway to develop materials with ultrahigh strength and superior ductility at economical material costs.

1. Introduction

Reduced activated ferrite martensitic (RAFM) heat-resistant steels are considered as potential structural materials for nuclear

* Corresponding authors.
E-mail addresses: clzhoujinhua@163.com (J.H. Zhou), roritchie@lbl.gov (R.O. Ritchie).

https://doi.org/10.1016/j.ijplas.2023.103813
Received 6 October 2023; Received in revised form 15 November 2023;
Available online 18 November 2023
0749-6419/

fusion energy reactors due to their superior thermal conductivity, thermal expansion, and resistance to radiation-induced swelling and helium embrittlement as compared to austenitic stainless steels (Peng et al., 2018; Liu et al., 2019). Prior to 1980s, the austenitic and ferritic stainless steels were mainly used to the cladding structural materials in the nuclear fusion reactors (Noda et al., 1988). However, after long-term service, these steels tend to show high levels of radioactivity which is difficult to handle. Bloom et al. (1984) first proposed the concept of reduced activated materials. They believed that after irradiation, the high radioactivity of a material mainly arises from the highly active elements in its composition. Accordingly, such active elements such as Ni, Nb, Mo, Co were restricted as additions to reduced activated materials, whereas low activity elements such as Ti, V, Ta, W could be added.

In 1989, Klueh et al. (2000) successfully prepared a 9Cr2WVTa steel and significantly reduced its radiation intensity after service. Subsequently, many countries developed different types of RAFM steels through adjustments of the chemical element composition of 9Cr2WVTa steel such as EUROFER 97 in Europe (Dethloff et al., 2014), F82H in Japan (Noh et al., 2016), and a China low activation martensitic (CLAM) steel in China (Tang et al., 2019). However, due to the relatively fixed elements of RAFM steel, there is no significant difference in the mechanical properties of different types of RAFM steel developed by the various countries. As the output power of nuclear fusion reactors is positively proportional to their reaction temperature (Zinkle et al., 2017), the low maximum operating temperature of RAFM steels has also become a major constraint on the further development of such nuclear reactors.

At present, the methods to further improve the room-temperature and high-temperature mechanical properties of RAFM steel are usually precipitation strengthening and subgrain strengthening (Li et al., 2017, 2023; Ritchie et al., 2011; George et al., 2019; He et al., 2021). Oxide dispersion strengthening (ODS) process can improve the room and high temperature mechanical properties of steels by introducing a large number of nanoscale oxide particles. However, due to the interaction between oxide precipitation and dislocations, it is easy to cause stress concentration and promote microcrack initiation, so the ductility of ODS steels is not ideal (Shi et al., 2019). In addition, the large degree of plastic deformation can also significantly refine the precipitation phase and subgrain size in these steels. For example Jin et al. (2018) prepared an ultrafine subgrained 9Cr2WVTa steel by multi-pass rotary-swaging and post-annealing to successfully increase the yield strength from 650 to 1100 MPa but the maximum elongation decreased from 25 % to 10 % due to the high stress concentration near the precipitation phase and subgrain boundaries. Unlike other structural materials, ductility is more important for RAFM steel. Due to its continuous exposure to irradiation during service, the radiation hardening acts to continuously reduce its ductility, such that excellent initial tensile ductility is particularly important for these steels (Peng et al., 2018; Liu et al., 2019). Accordingly, the critical issue at present is to find a process that can simultaneously improve both the strength and plasticity of RAFM steels.

Currently, one of the effective ways to simultaneously improve the strength and ductility in steels has been to use transformation-induced (TRIP) and twinning-induced (TWIP) plasticity effects (Chandan et al., 2022; Li et al., 2022). Deformation-induced martensite and nanotwins can absorb large amounts of energy, thus delaying the proliferation of dislocations and avoiding local stress concentrations (Wang et al., 2020; Tang et al., 2019). However, as both the TRIP and TWIP effects are characteristic of the austenitic structure, which has fewer interfaces and poorer radiation resistance (Yu et al., 2018), they are generally not suitable for RAFM steels. Another way to simultaneously improve strength and ductility is by refining the grain size (Lai et al., 2022; Tiamiyu et al., 2018; Yin et al., 2023), although this method is also not ideal as the binding force between the high-angle grain boundaries will significantly decrease under elevated-temperature service conditions that can lead to intergranular sliding and a significant reduction in high-temperature strength (Zhang et al., 2022b; 2022c; Jiao et al., 2019; Tian et al., 2016). In addition, the heterostructure (nano grains in a micro grain structure) could also simultaneously improve the strength and ductility of steel, where the strength results from the nano grains and the ductility from the micro grains. However, due to the poor high-temperature strength of nanograins, such heterostructures are also not ideal for RAFM steels (Zhu et al., 2023).

An alternative approach to generating strength and ductility is to create a lamellar grain structure, as recently presented by Li et al. (2023) and Liu et al. (2020). However, their research on lamellar structures is focused on TRIP steels, and due to the complex phase transition in these alloys, the influence of the lamellar structure on the strength and ductility cannot be clearly explained. In this study, we prepared a CLAM steel (which only has a ferritic microstructure) with a layered structure through a hot rolling and low-temperature tempering process. The room temperature and 600 °C tensile properties of this steel were tested and indicated that the layered structure exhibits a new ductility mechanism. Based on these observations, we analyzed the crack propagation behavior of this layered CLAM steel under tensile conditions at ambient and high temperatures, in order to clarify the ductility mechanisms dominant in such layered structural materials.

2. Methods

In this study, we prepared a layered CLAM steel through hot rolling and low-temperature tempering. The mechanical properties of the steel at room and 600 °C were evaluated using uniaxial tensile tests. The microstructure of the steel before and after stretching was characterized by optical microscopy (OM), scanning electron microscopy (SEM) in conjunction with electron backscatter diffraction (EBSD), and transmission electron microscopy (TEM).

2.1. *Materials*

The CLAM steel, with a chemical composition of Fe - 8.91 % Cr - 1.4% W - 0.54% Mn - 0.15 % Ta - 0.15 % V- 0.09 % C - 0.06 % Si (wt.%), was melted in a vacuum induction furnace and then cast as ingots of 65 mm × 65 mm × 80 mm in dimensions. The ingots were solution treated in an air furnace at 1200 °C for 2 h to homogenize the microstructure and completely dissolve primary carbides, prior to hot and then warm rolling to extensively elongate the prior-austenite grains along the rolling direction. With a starting hot rolling temperature of 1150 ℃, the ultimate rolling temperature was 1050 ℃ with a deformation rate of 45 %; with the starting warm rolling temperature at 850 ℃, the ultimate rolling temperature was 800 ℃ with a deformation rate of 60 %. During subsequent cooling, the austenite was completely transformed into martensite to form a laminated martensite microstructure (Fig. 1). Finally, the steel was tempered for 30 min at 700 ℃ to transform the martensite into ferrite and allow the full precipitation of carbides, thereby increasing the ductility of the steel. By comparison, the current heat-treatment process for the RAFM steel is hot rolling, followed by austenitizing and tempering treatments to achieve an equiaxed grain structure (Wang et al., 2015; Dethloff et al., 2014; Noh et al., 2016; Tang et al., 2019).

2.2. Uniaxial tensile testing

Uniaxial tensile properties were measured at room temperature (RT) and at 600 ℃, using a constant displacement rate of 0.5 mm / min under displacement control. Dog-bone shaped specimens measuring 15 mm × 5 mm × 1.5 mm were obtained from the middle of the as-rolled steel sheets along the rolling direction (RD) using electrical discharge machining. The uniaxial tension tests were performed on an AGS-X plus PC-controlled mechanical testing system manufactured by Shimadzu Co. Ltd, Japan in accordance with ASTM E8-04 Standard. A contactless laser Xtens Compact laser extensometer was utilized to measure the tensile strain of the material. The reported data represent the average of three separate tests.

2.3. Microstructure characterization

The phase diagram of the material was simulated using JMATPRO software, developed by Sente Software in the UK, which can simulate the phase diagram and mechanical properties of metals. The microstructure of the as-prepared steels was characterized by OM and SEM in conjunction with EBSD. To prepare the specimens for OM and SEM observations, they were mechanically polished and etched with Vilella reagent, comprising 1 g picric acid, 5 ml hydrochloric acid, and 100 ml ethanol. The specimens for EBSD observations were also mechanically polished and electropolished to remove the surface damage caused by grinding. The electrolyte used for electropolishing was composed of 11 vol.% perchloric acid and 89 vol.% ethanol. OM observations were carried out with a GX71 / Leica Dmirm optical microscope with EBSD analyzes conducted using a field emission scanning electron microscope (SU-70 Hitachi field-emission SEM, Japan) at a voltage of 15 kV and tilt angle of 70° The selected scanning step was 0.1 μm, with an analyzed area of 1.5 × 1.0 mm^2 for each specimen. Evaluation of the EBSD data was carried out with orientation imaging microscopy (OIM, HKL-Channel 5) software. To identify low-angle (LAGBs: 2–15°) and high-angle grain boundaries (HAGBs: >15°), band contrast plus grain-boundary (GB) maps were utilized. The boundaries with an orientation difference below 2° were excluded.

Microstructural characterization of the samples was performed using a Tecnai G2 transmission electron microscope (TEM) at an accelerating voltage of 200 kV. Specimens were mechanically polished to a thickness of ~50 μm and then further thinned at 20 V and -20 ℃ using a twin-jet electrochemical polisher in an electrolyte that consisted of 10 vol.% perchloric acid and 90 vol.% ethanol.

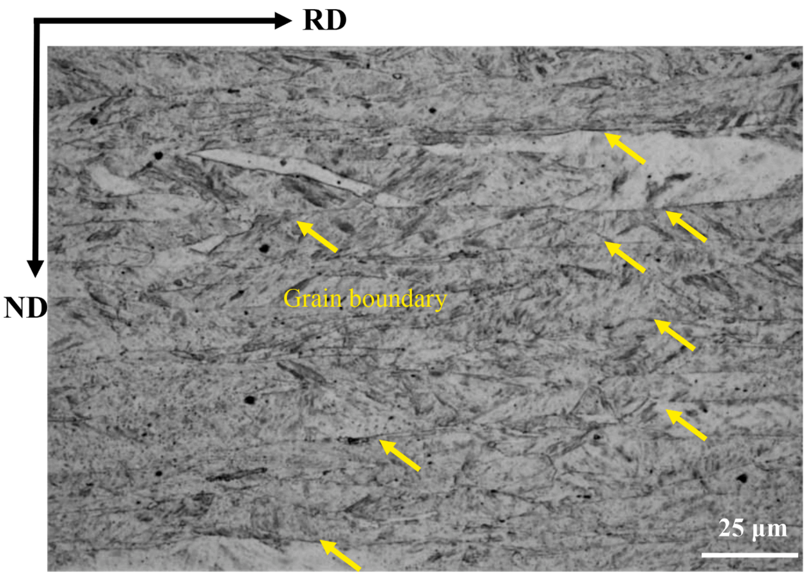

Fig. 1. Microstructure of the laminated martensite microstructure of the CLAM steel after rolling along the rolling direction (RD) and normal direction (ND).

3. Results

3.1. Microstructure characterization

Fig. 2a and b shows the EBSD orientation map, band contrast and the grain boundary map of the CLAM steel after the rolling and tempering treatment. The steel exhibits a lamellar structure of high-angle grains, with an average width and length of 2 and 5 μm with the length direction parallel to the rolling direction. A significant amount of subgrain structures can be observed inside the grain boundaries of the high-angle grains. The TEM morphology of these grains and subgrains is shown in Fig. 2c and d; these images also indicate the many subgrains inside the grains. A large number of precipitates are distributed on the grain boundaries and subgrain boundaries, shown by the white particles in Fig. 2d. The X-ray diffraction (XRD) patterns of the tempered steel are shown in Fig. 3, where it is evident that there are four diffraction peaks in the steels - (110), (200), (211) and (220) - which are all from the ferrite.

Fig. 4 shows the TEM images of the morphology of ferrite laths and particles in the CLAM steel. The laths, with an average thickness of ~170 nm, are parallel to each other within their colonies; their boundaries are decorated with a short rod-like precipitate phase with an average size of ~30 nm and a total volume fraction of 0.25 (determined from its area fraction in the TEM observations) (Fig. 4a and

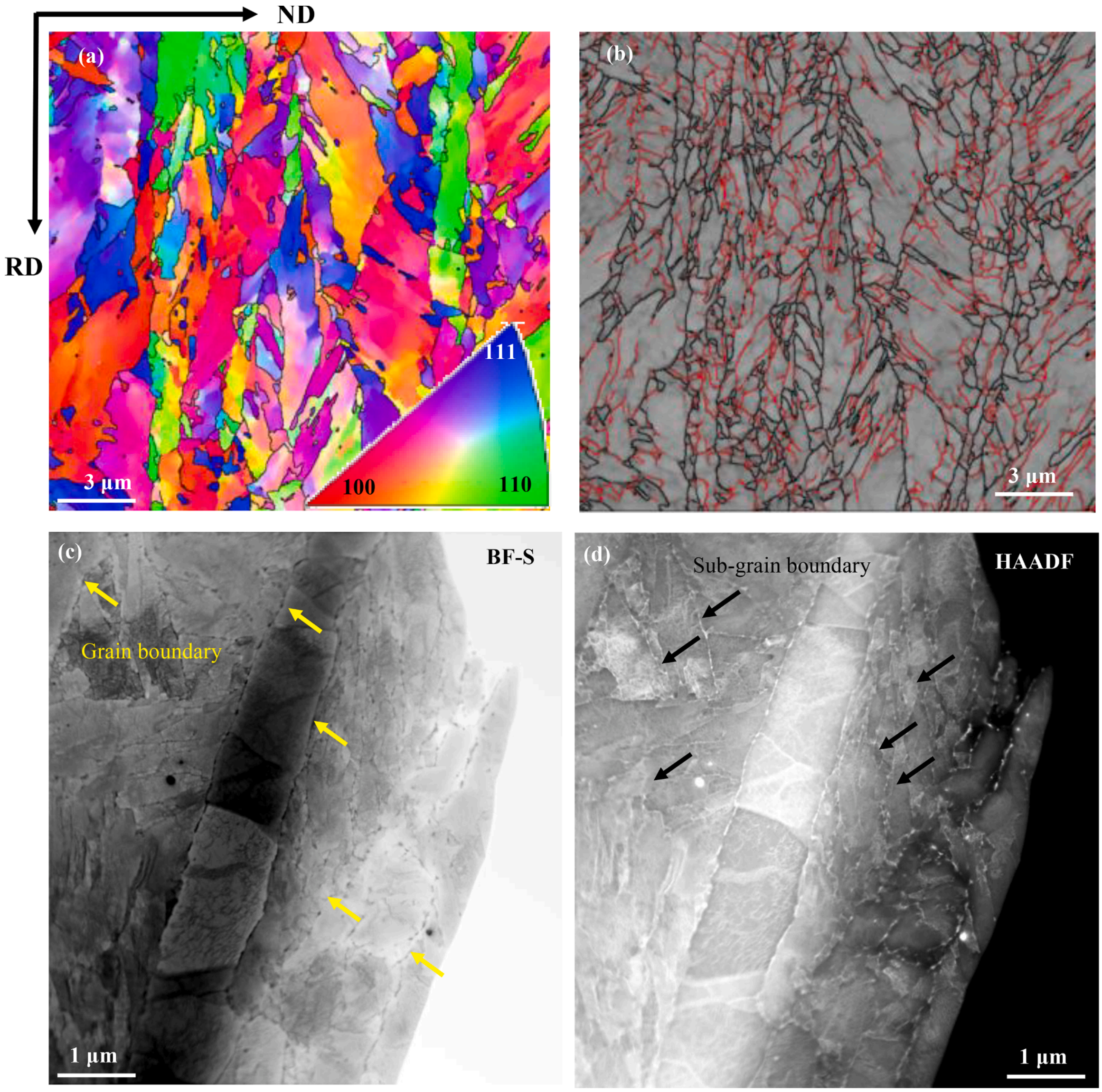

Fig. 2. Microstructure of the present CLAM steel. (a) Orientation maps, band contrast and (b) grain boundary maps obtained from electron backscatter diffraction (EBSD) for the lamellar CLAM steel. Grains with {100}, {111}, and {110} orientations are marked respectively in red, blue and green (inset in a). Low-angle grain boundaries (LAGBs, 2–15°) and high-angle grain boundaries (HAGBs, >15°) indicated by red and black lines. (c, d) TEM images of a grain, sub-grain and particles morphology.

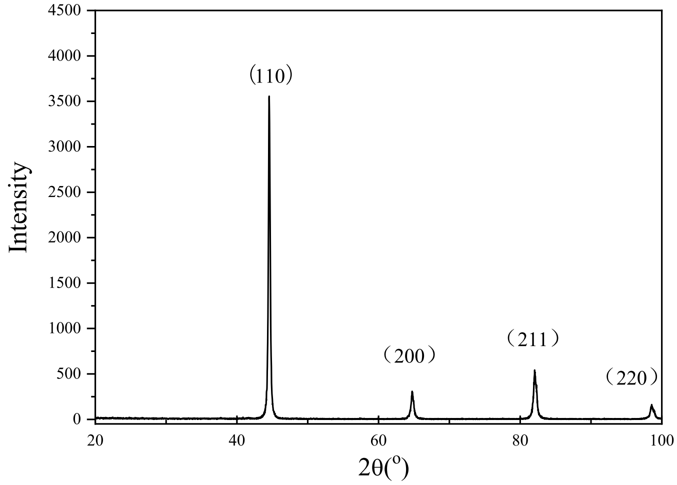

Fig. 3. X-ray diffraction (XRD) patterns shows the single-phase ferrite structure for the CLAM steel under study.

b). Energy spectrum analysis (Fig. 4c–h) revealed that the precipitate phase is $M_{23}C_6$ carbide, which is rich in Cr, Mn, Ta, and W. Fig. 5a shows the HRTEM image of the fine $M_{23}C_6$ carbide and the ferrite. Observations reveal that the ferrite had an inter planar spacing of 0.205 nm between the neighboring (-110) *bcc*-Fe planes (Fig. 5d), while for $M_{23}C_6$ carbide the spacing between neighboring (-110) planes was 0.246 nm (Fig. 5b). This suggests that the interface between fine particles and the matrix was incoherent. Accordingly, the $M_{23}C_6$ carbide can effectively hinder the movement of dislocations in the ferrite, but the large mismatch between the carbides and ferrite also makes it easy to generate stress concentration at the $M_{23}C_6$ carbide /ferrite interface, leading to the initiation of micro-cracks. Fig. 5c and e shows the diffraction pattern of the carbide and ferrite, which confirms that the precipitated phase is $M_{23}C_6$ carbide, and that the tempered CLAM steel has a ferritic structure. Although the size of the ferrite laths and $M_{23}C_6$ carbides in traditional CLAM steels are usually larger than 300 nm and 100 nm, respectively (Chen et al., 2023; Zhao et al., 2018; Wang et al., 2019; Zhou et al., 2021), the smaller size of the laths and carbides in the current steel is due to the short-term tempering process used in this experiment.

The primary chemical components of the ferrite lath and carbides, shown in Fig. S4i, indicate that the main elements in the ferrite are Fe and Cr, with other elements accounting for ~3 at.%. The volume fraction of other elements in the carbides is ~12 at.%, indicating that the alloying elements in this steel are fully precipitated after the tempering treatment. As low content alloying elements in the matrix do not significantly strengthen the ferrite, it displays excellent plasticity. (For higher Cr content in the ferrite, the solid solution strengthening between Cr and Fe can be ignored, as the atomic size of Cr is similar to that of Fe).

It should be noted that the microstructure of traditional CLAM steels invariably involves a large number of small, dispersed MX carbides rich in V and Ta within the ferrite lathes (Chen et al., 2023; Zhao et al., 2018; Wang et al., 2019; Zhou et al., 2021). However, such carbides were not observed in the present steel. Fig. 6 shows a phase diagram of the CLAM steel using JMatPro software (Wang et al., 2022). One can see that the precipitation temperature of the MX carbides was high at 1260 ℃, suggesting that they could precipitate at the high temperature, which typically occurs during the austenitizing stage. However, our process does not involve a solution treatment, resulting in the lack of any precipitation of MX carbides. Indeed, the precipitation temperature of the $M_{23}C_6$ carbides is 850 ℃, which is remarkably lower than that of MX carbides; accordingly, the MX carbides can precipitate during the tempering stage, although the lower tempering temperature of 730 ℃ in this study made the size of the carbides very small. From JMatPro calculations, there should be 2 wt.% of Laves phase, although no such phases were detected in this study because the short duration of the holding time would retard their formation. However, as the shortest precipitation time for Laves phases was reported to be ~10 h at 650 ℃ in a 9Cr (1–4 W) steel (Abe et al., 1991), it is probable that long aging times could promote their precipitation (Wang et al., 2019), a phenomenon which would likely degrade ductility.

3.2. Tensile properties

The engineering stress-strain curves of the lamellar CLAM steel, shown in Fig. 7a, indicate that at room temperature alone the rolling direction (RD), the yield strength (σ_y) is 900 ± 10 MPa, the tensile strength (σ_{TS}) is 1025 ± 10 MPa, and the maximum elongation is 18 ± 1 %; these values are respectively 480 ± 10 MPa, 500 ± 10 MPa and 20 ± 1 % at 600 ℃. While at room temperature along the normal direction (ND), the values of σ_y, σ_{TS} and maximum elongation are 900 ± 10 MPa, 1025 ± 10 MPa, and 8 ± 1 %; these values are respectively 460 ± 10 MPa, 480 ± 10 MPa and 12 ± 1 % at 600 ℃. Clearly, there is little significant change in the strength of the material in the RD and ND directions, but the elongation in the RD direction is significantly higher than that in the ND direction. The morphology of the tensile samples after fracture at room temperature and 600 ℃, shown in Fig. 7b, reveal significant necking and a longitudinal tear of ~2 mm near the fracture surface at room temperature alone the RD. Significant necking was also observed at 600 ℃, but no visible longitudinal tearing was seen. Along the ND, neither necking nor longitudinal tearing were observed at room

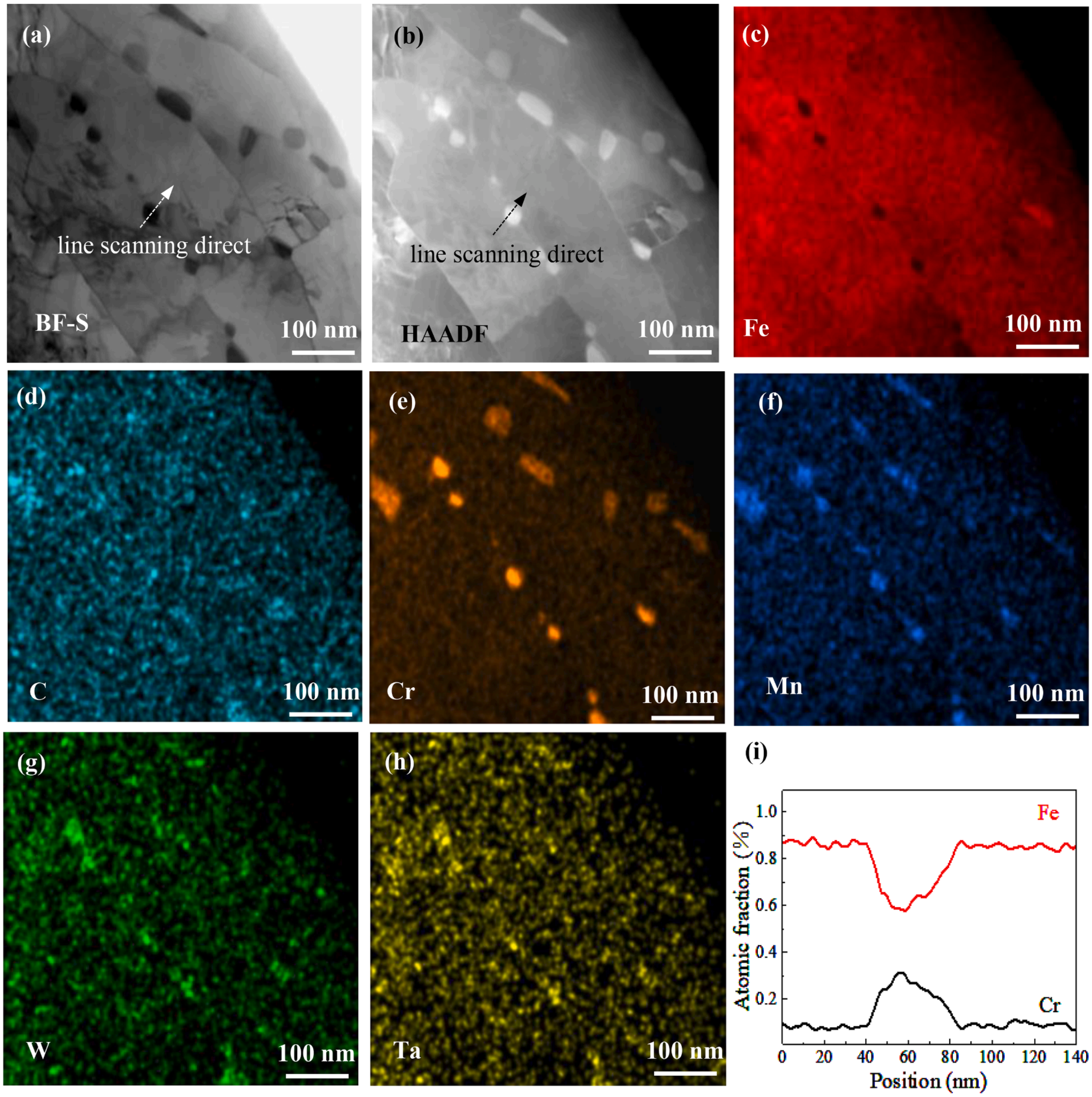

Fig. 4. Microstructure of the ferrite lath and $M_{23}C_6$. (a, b) TEM images of a ferrite lath and $M_{23}C_6$ carbide morphology; (c-h) energy dispersive spectroscopy (EDS) analysis for the ferrite laths and $M_{23}C_6$ carbides; (i) primary chemical components of the ferrite laths and $M_{23}C_6$ carbides.

temperature and at 600 ℃, with the steel exhibiting brittle fracture characteristics.

Fig. 7c and d shows a comparison of the yield strength and maximum elongation at room temperature and 600 ℃ between the laminated CLAM steel, the ODS steel (Shi et al., 2019; Klueh et al., 2005; Li et al., 2011; Zhao et al., 2017; Yan et al., 2018), and the traditional RAFM steel (Chen et al., 2015; Jin et al., 2018; Tan et al., 2016; Xue et al., 2019; Zhou et al., 2020, 2021). Due to a large number of dispersed nanoscale oxide particles, the ODS steel exhibits the highest strength at room temperature and at 600 ℃. However, owing to the entanglement between dislocations and these particles, local stress concentrations during the tensile process can readily occur, resulting in poor ductility. The preparation process of the ODS steel is oxide metallurgy, which includes ball milling, mechanical alloying, hot isostatic pressing, hot rolling, and heat treatment processes. Ball milling and mechanical alloying processes can easily cause uneven powder mixing, resulting in an inhomogeneous distribution of chemical elements in the steel. Compared with the hot rolling and heat treatment process of RAFM steel, the complex preparation process of ODS steel also can significantly increase its production costs (Shi et al., 2019). For the traditional RAFM steel, its coarse subgrains and carbides decrease the resistance to dislocation movement to result in good ductility, but its strength is relatively low. Owing to strengthening from the grain boundaries, subgrain boundaries and precipitation, the CLAM steel exhibits extremely high strength and, due to its unique delamination ductility mechanism along the RD, it also has high ductility. Thus the RD layered structure CLAM shows a good match of strength and plasticity at room temperature and 600 ℃ that current processing cannot readily achieve.

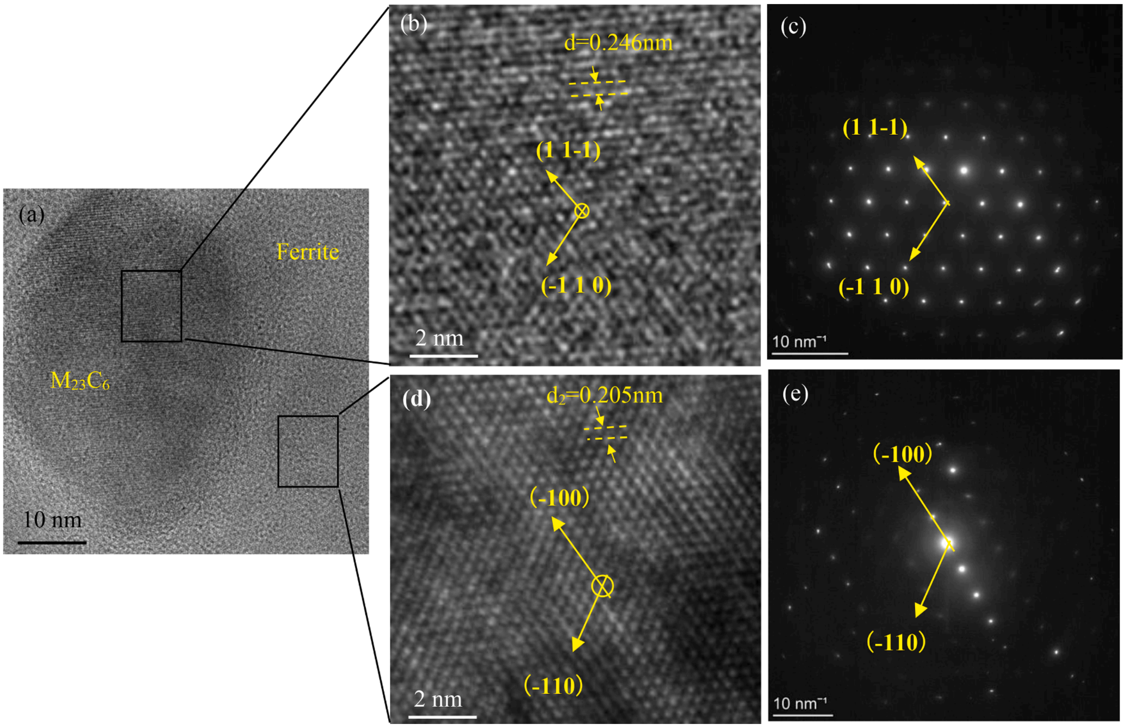

Fig. 5. High resolution transmission electron microscope (HRTEM) image of the ferrite laths and $M_{23}C_6$ carbides. (a) HRTEM image showing the morphology of a $M_{23}C_6$ carbide in the CLAM steel; (b,d) is the close observation exhibiting the crystal lattice and planar spacing in the carbide and ferrite; (c,e) is the diffraction pattern of the carbide and ferrite.

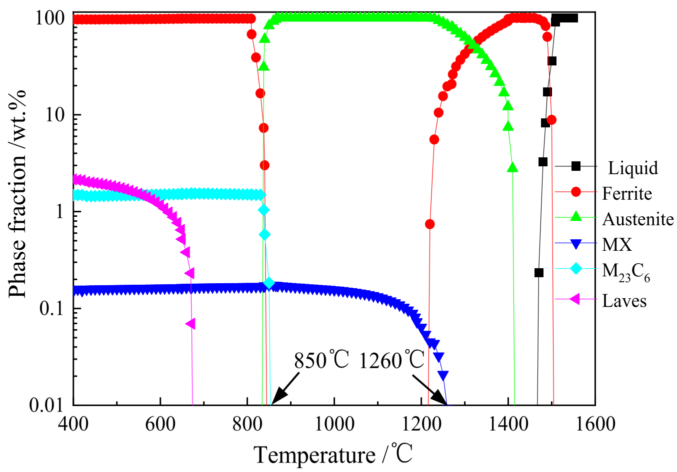

Fig. 6. Phase diagram for CLAM steel calculated by JMatPro software (Wang et al., 2022).

4. Discussion

4.1. Room temperature strength mechanisms

The strengthening mechanisms of metal materials are usually related to grain-boundary (Yin et al., 2023), subgrain (Zhang et al., 2023), precipitation (Xiao et al., 2023), dislocation (Li et al., 2022), and solid-solution (Fang et al., 2022) strengthening. However, in this experiment after tempering, the alloy elements in the steel were basically fully precipitated (Fig. 4l), and dislocations were highly limited (Fig. 4a and b), such that solid-solution and dislocation strengthening can be essentially ignored. Thus, the strength in the lamellar CLAM steel is generated primarily from grain boundaries, subgrain boundaries, and $M_{23}C_6$ carbides.

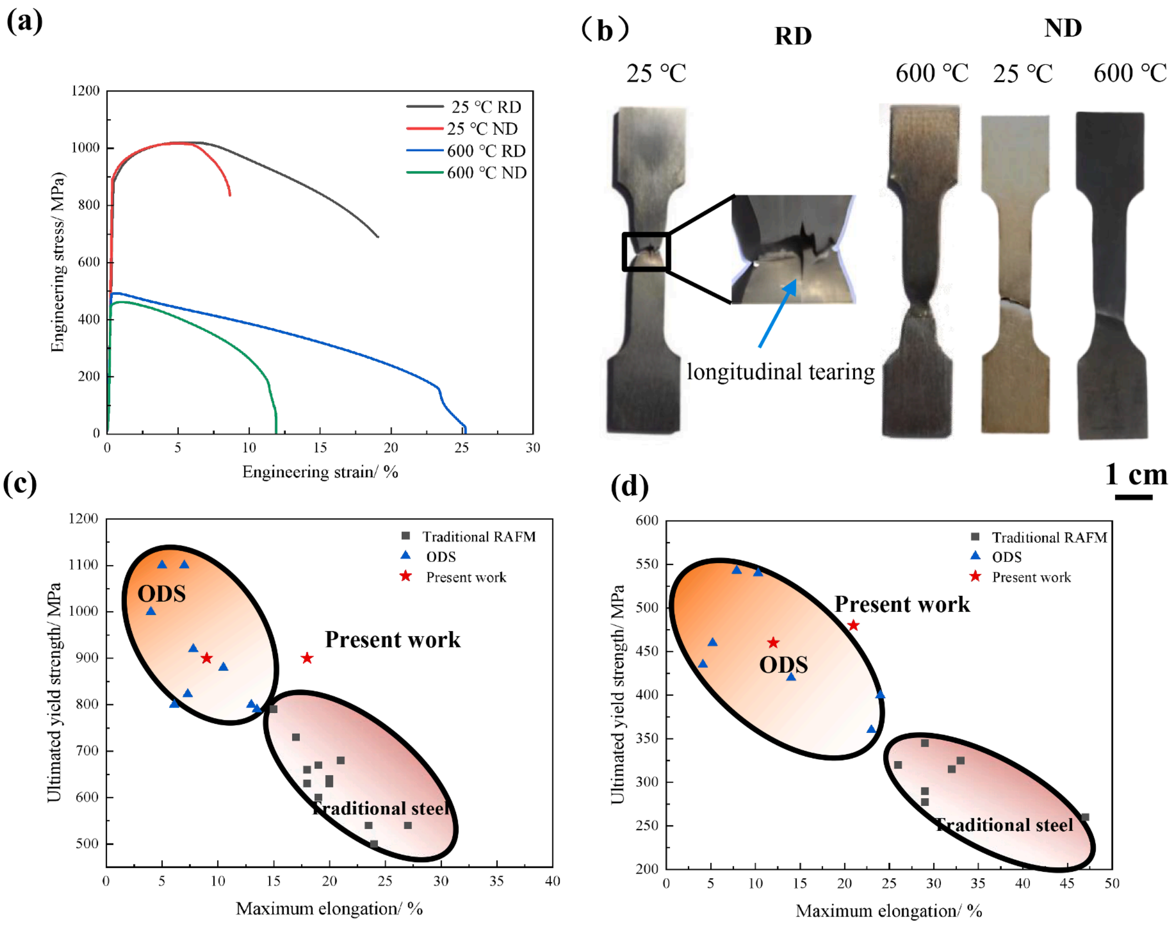

Fig. 7. Tensile properties of the present steel. (a) Engineering stress-strain curves for the lamellar CLAM steel tested at room temperature and 600 ℃; (b) macroscopic morphology of the steel samples after tensile fracture at room temperature and 600 ℃; (c and d) comparison of the yield strength and maximum elongation at room temperature and 600 ℃ between laminated CLAM steel, ODS steel (Shi et al., 2019; Klueh et al., 2005; Li et al., 2011; Zhao et al., 2017; Yan et al., 2018), and traditional RAFM steel (Chen et al., 2015; Jin et al., 2018; Tan et al., 2016; Xue et al., 2019; Zhou et al., 2020, 2021).

4.1.1. *Boundary and sub-boundary strengthening*

The interaction of dislocations with grain boundaries and subgrain boundaries is shown in Fig. 8a and b. Clearly there are many subgrains within a grain, and both grain boundaries and subgrain boundaries can effectively hinder the movement of dislocations.

The grain-boundary strengthening, $\Delta\sigma_{GB,}$ can be calculated using the Hall-Petch equation (Petch et al., 1953) as follows:

$$\Delta\sigma_{GB} = k_{hp}d^{-1/2} \tag{1}$$

where $k_{h\text{-}p}$ is a constant related to the interaction between the grain boundary and the dislocations, with a value of 0.62 MN m$^{-1.5}$ (Li et al., 2007), and d is the average grain size (here the high-angle grain diameter). Clearly, as the grain size decreases, grain-boundary strengthening continues to increase. The grain size of the lamellar CLAM steel was ~3.5 μm, whereas the traditional RAFM steel is usually larger than 5 μm (Chen et al., 2015; Jin et al., 2018; Tan et al., 2016; Xue et al., 2019; Zhou et al., 2020, 2021). Consequently, $\Delta\sigma_{bs}$ can be estimated to be ~365 MPa for the lamellar CLAM steel and less than 270 MPa for the traditional RAFM steel (Fig. 9).

The subgrain strengthening, $\Delta\sigma_{SGB}$, can be calculated using (Tan et al., 2016):

$$\Delta\sigma_{SGB} = MGb/\lambda \tag{2}$$

where M is the Taylor factor with a value of 3, G is the shear modulus (76 GPa for steel), b is the Burgers vector (2.85 × 10^{-10} m), and λ is the subgrain size (Tan et al., 2016). Clearly, the improvement in strength due to subgrain boundaries is increased with a reduction in the subgrain size. The grain size of the lamellar CLAM steel was ~170 nm; for the traditional RAFM steel, the grain size is usually larger than 300 nm (Chen et al., 2015; Jin et al., 2018; Tan et al., 2016; Xue et al., 2019; Zhou et al., 2020, 2021). Consequently, $\Delta\sigma_{GB}$ can be estimated to be 380 MPa for the lamellar CLAM steel and less than 215 MPa for the traditional RAFM steel (Fig. 9).

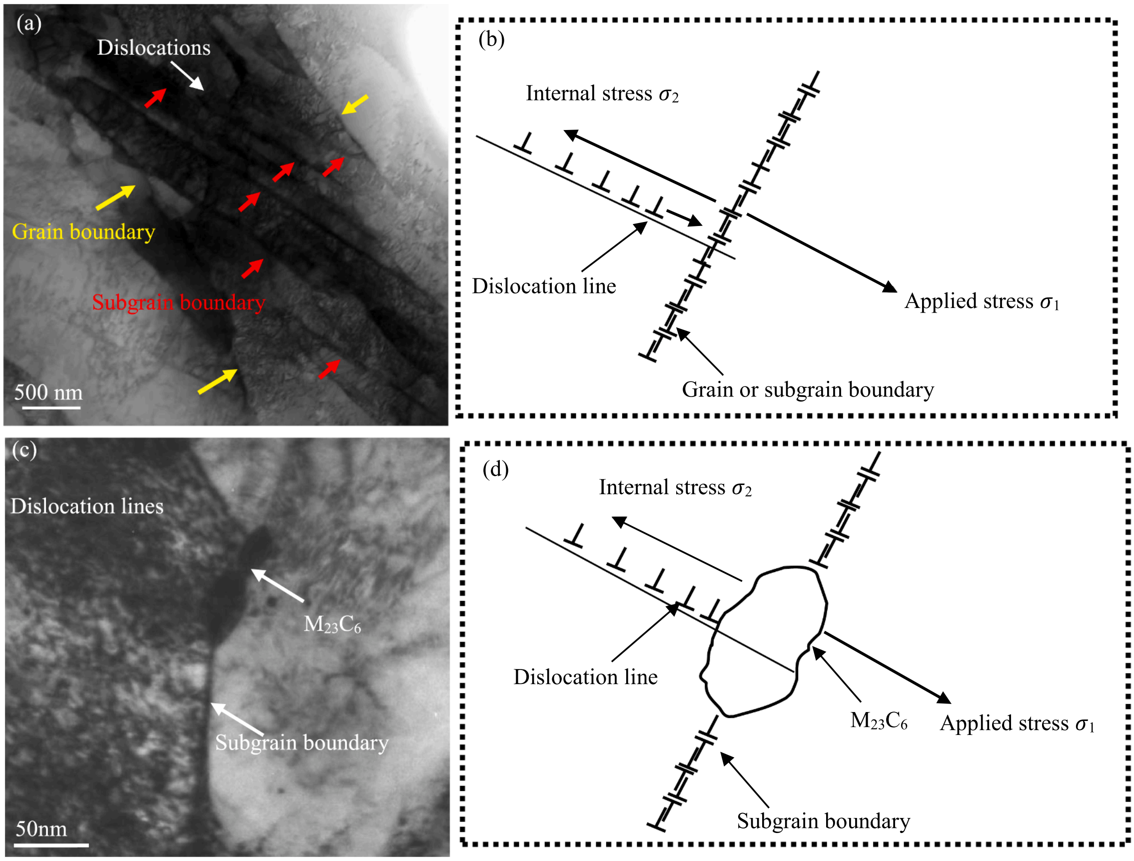

Fig. 8. Interaction between the interfaces, $M_{23}C_6$ carbides and dislocations in the deformed steel. (a,b) Typical TEM micrographs and schematic diagram of the interaction between the interfaces and dislocations. (c, d) Typical TEM micrographs and schematic diagram of the interaction between the $M_{23}C_6$ carbides and dislocations.

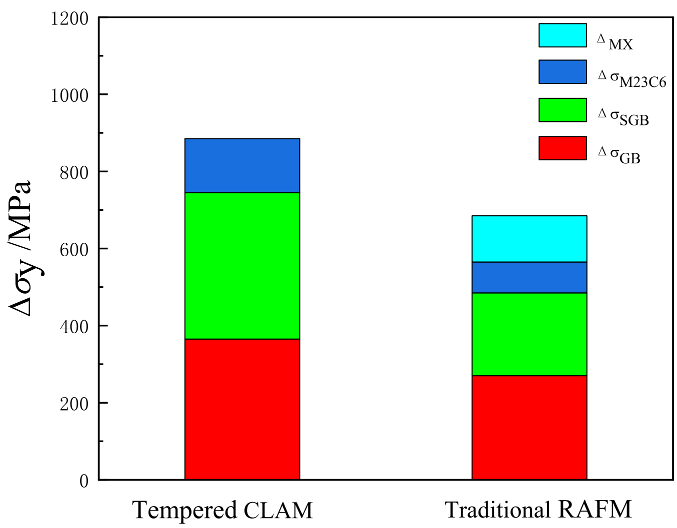

Fig. 9. A schematic diagram showing calculated strengthening contributions for the tempered CLAM steel and traditional RAFM steels.

4.1.2. Precipitation strengthening

TEM imaging and the corresponding schematic illustration in Fig. 8c and d clearly show that the $M_{23}C_6$ carbides were mainly distributed at the grain and subgrain boundaries; this means that they were difficult for dislocations to bypass such that the dislocations were accumulated in the vicinity of these carbides. The dislocations near the carbides accordingly would generate an internal stress which is opposite to the external stress, thereby hindering the movement of dislocations in the vicinity of the subgrains. The resulting strengthening of $M_{23}C_6$ carbides, Δσps-$M_{23}C_6$, can be estimated using the dispersed barrier hardening (DBH) model (Cho et al., 2015) because of the large size of the $M_{23}C_6$ carbides, viz:

$$\Delta\sigma_{ps-}M_{23}C_6 = M\alpha Gb\sqrt{Nd'}, \tag{3}$$

where α is a barrier strength factor (1.0 for voids), G is shear modulus (76 GPa), N is density and d' is the average size of the $M_{23}C_6$ carbides (Cho et al., 2015). The particle size and density fraction of $M_{23}C_6$ carbides in the lamellar CLAM steel were respectively 30 nm and 1.5×10^{20} m^{-3} The $M_{23}C_6$ carbides in traditional RAFM steel are usually larger than 100 nm with a fraction of less than 1.5×10^{19} m^{-3} (Chen et al., 2015; Jin et al., 2018; Tan et al., 2016; Xue et al., 2019; Zhou et al., 2020, 2021). Consequently, $\Delta\sigma_{ps-}M_{23}C_6$ can be calculated to be ~140 MPa for the lamellar CLAM steel and about 80 MPa for the traditional RAFM steel (Fig. 9).

In addition to $M_{23}C_6$ carbides, there are usually MX type carbides with a size of about 20 nm and a volume fraction of 0.2 % in traditional RAFM steel (Chen et al., 2015; Jin et al., 2018; Tan et al., 2016; Xue et al., 2019; Zhou et al., 2020, 2021). These carbides exist inside the subgrains and strengthen the steel through an Orowan by-passing mechanism (Sasaki et al., 2011; Lucas et al., 1993), contributing approximately 120 MPa to the strength of the steel. However, due to the lack of a solid-solution treatment stage, MX type carbides were not observed in the lamellar steel in this work.

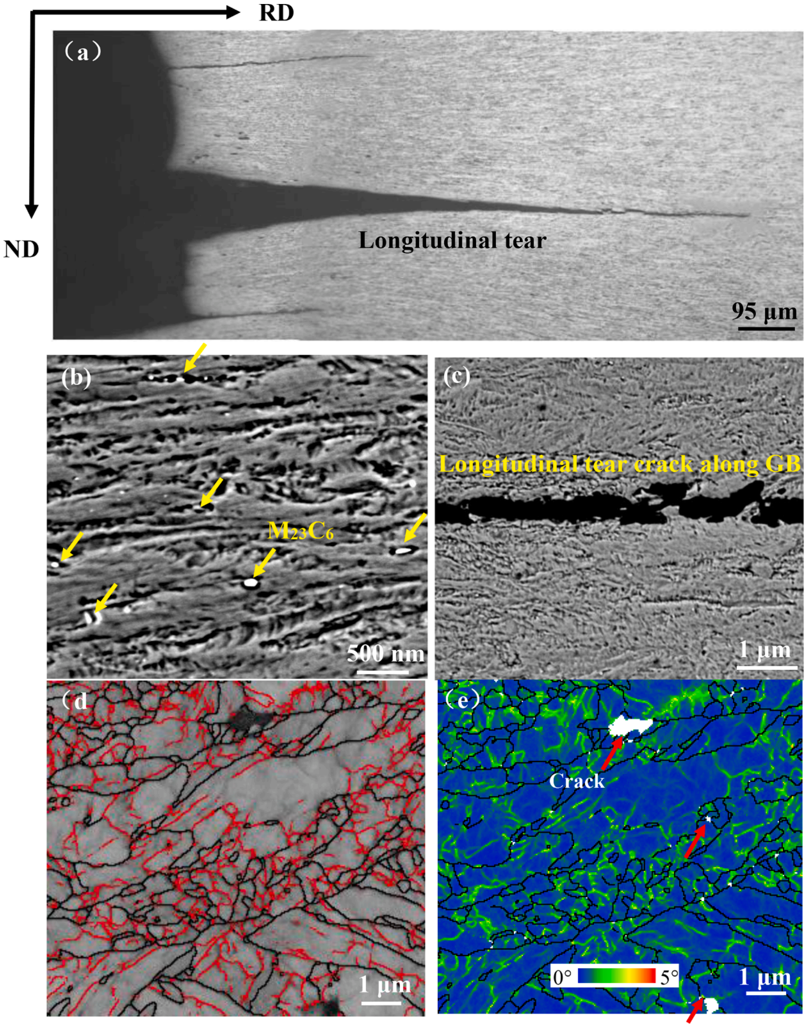

Fig. 10. Room temperature ductility mechanisms for the CLAM steel in rolling direction. (a) Optical microscopy images of the through-thickness section normal to the room temperature fracture surface showing the macroscopic morphology of a longitudinal tear and the morphology of crack propagation; (b and c) scanning electron microscopy images showing the crack initiation and propagation; (d) band contrast and grain boundary maps near the fracture surface obtained from electron backscatter diffraction (EBSD). (**e**) A map of the kernel average misorientation (KAM) derived from EBSD data in {100}, {111}, and {110} orientations to illustrate the local misorientation across the grains.

Fig. 9 shows a comparison of the calculated strengths of the lamellar CLAM and traditional RAFM steels. The calculated strength of lamellar CLAM steel is 885 MPa, which is close to its measured yield strength of 900 MPa. The calculated yield strength of the traditional RAFM steel is 680 MPa, compared to values in the literature (Chen et al., 2015; Jin et al., 2018; Tan et al., 2016; Xue et al., 2019; Zhou et al., 2020, 2021) between 550 and 700 MPa (Fig. 7c). Clearly, the higher yield strength of the layered CLAM steel, compared to traditional RAFM steel, can be largely related to the strengthening from the subgrain boundaries and $M_{23}C_6$ precipitation. However, for traditional RAFM steel, further improvements in the subgrain and carbide strengthening can markedly increase the strength but will also significantly compromise the ductility, as shown in Fig. 7c. This is the advantage of the layered CLAM steel as its unique layered structure allows it to enhance strength without reducing ductility.

4.2. RD room temperature ductility mechanisms

For the RD lamellar structured CLAM steel, its crack propagation mechanism is significantly different. Fig. 10a shows the optical microscopy morphology of the through-thickness section normal to its fracture surface, showing a 1 mm long longitudinal tear near the surface. Fig. 10b and c shows the microcracks initiation and propagation morphology for the steel, where it is apparent that many microcracks exist near the $M_{23}C_6$ carbides, suggesting that the microcracks mainly originated from these carbides in the presence of an applied load. The initiation of microcracks is closely related to stress concentration. As carbides can effectively hinder the movement of dislocations, stress is easily concentrated on the $M_{23}C_6$ carbides / ferrite interface. Moreover, due to the large mismatch between the carbides and the ferrite, microcracks are readily initiated at the these carbide/ferrite interfaces. Once the microcracks form, they tend to propagate along the grain and subgrain boundaries, due to the high stress concentration on these boundaries. Fig. 10d and e shows the band contrast and grain boundary and kernel average misorientation maps near the fracture surface obtained from electron backscatter diffraction (EBSD) analysis. Clearly, a higher local misorientation is present at the grain boundaries and subgrain boundaries, which corresponds to the distribution of dislocations along these interfaces (Fig. 8a), such that a large number of microcracks propagate and accumulate near the high-angle grain boundaries (shown in the white area marked by the red arrows in Fig. 10d). This indicates that both grain boundaries and subgrain boundaries can effectively impede the movement of dislocations during room temperature tension, while microcracks will preferentially extend along the grain boundaries due to the high degree of mismatch between the atoms at the grain boundaries and the grain. The morphology of the tensile fracture surface, which represents results from three specimens, is shown in Fig. 11a and b, where longitudinal tears with a maximum width of 125 μm can also be observed at the center of the fracture surface. The transverse dimension of these microcracks is significantly smaller than their longitudinal dimension, indicating that during their propagation, their transverse expansion rate is significantly slower than their longitudinal expansion rate. In addition to the main tear crack, only a small amount of fine dimples was observed in other parts of the fracture surface.

Fig. 12a shows a schematic diagram of the tensile microcrack propagation at room temperature in the RD lamellar CLAM steel. Firstly, due to the high degree of mismatch between the atoms at the $M_{23}C_6$ carbide/ferrite interface (Fig. 5), microcracks will preferentially initiate near the $M_{23}C_6$ carbides and then, due to the significant lattice distortion at the grain boundaries, will first extend to the grain boundaries and then further propagate along them (Zhang et al., 2022). Fig. 12aI shows the force analysis performed at the point of microcrack propagation. During the stretching process, when a microcrack propagates it cannot be subjected to tensile stress as microcracks are essentially empty spaces. However, the stress can act on the boundary between the microcrack and the ferrite, leading to further microcrack advance. The external stress F can be decomposed into the σ_1 and σ_2 stresses along the microcrack boundary direction. Further decomposition of these σ_1 and σ_2 stresses can yield longitudinal tensile stresses σ_{1y} and σ_{2y} and transverse compressive stresses σ_{1x} and σ_{2x} acting on the microcrack boundary. The longitudinal tensile stresses σ_{1y} and σ_{2y} can cause transverse

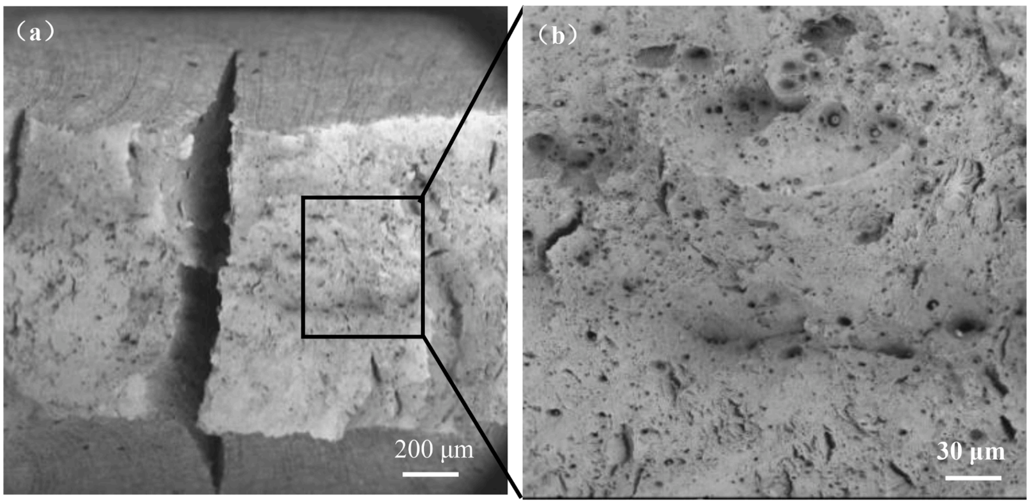

Fig. 11. Morphology of the room temperature tensile fracture surface of the CLAM steel in the rolling direction (a, b) at room temperature.

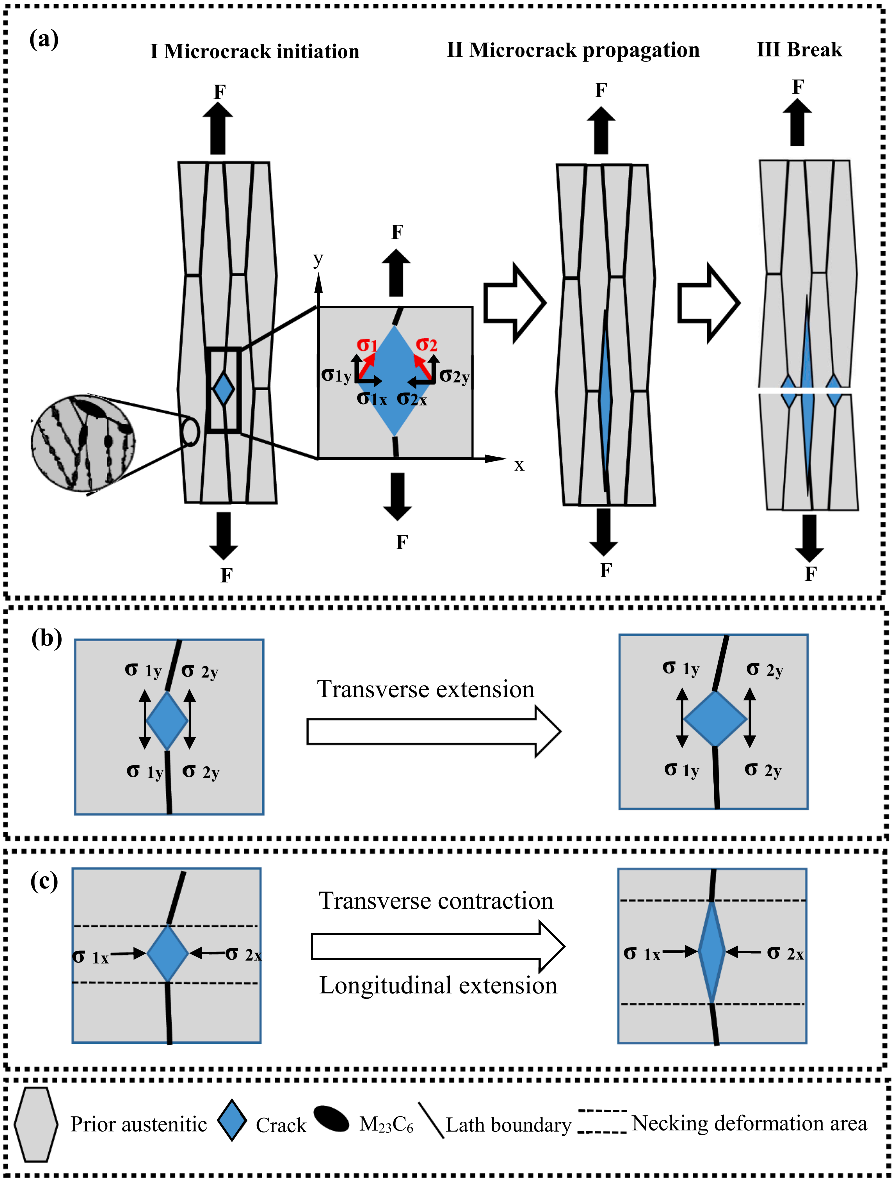

Fig. 12. Schematic diagram for the room temperature ductility mechanisms in the rolling direction. (a) Tensile crack propagation in the lamellar CLAM steel; (b and c) the propagation of a crack under tensile conditions.

microcrack propagation, while the transverse compressive stress σ_{1x} and σ_{2x} can induce necking in the material.

Subsequently, microcracks tended to propagate laterally under the longitudinal tensile stresses σ_{1y} and σ_{2y}, as shown in Fig. 12b. Under the transverse compressive stresses σ_{1x} and σ_{2x}, the material undergoes necking. In addition to the necking of the material, the transverse compressive stress will also act on the microcrack, causing it compress transversely inward. Due to the conservation of the microcrack volume, the transverse shrinkage will inevitably lead to its longitudinal expansion, as shown in Fig. 12c. Therefore under the tensile stress, the longitudinal expansion speed of the microcracks is significantly greater than the horizontal expansion speed, leading to the formation of longitudinal tears. Additionally, in this experiment, the grains of the steel exhibited a layered structure, with the grain elongation direction parallel to the tensile stress direction. The poor matching between grain boundaries and the grains further promoted longitudinal microcrack propagation. Additionally, the small degree of distortion in the grains also inhibited transverse microcrack expansion, eventually resulting in visible macroscopic longitudinal tearing (Fig. 12aII). This process also corresponds to the plane-strain crack propagation process. When the stress intensity factor K_I of the material exceeds its fracture toughness K_C, cracks will initiate and propagate. The stress intensity factor K_I can be represented by Irwin et al. (1957) as:

$$K_I = Q\,\sigma\sqrt{\pi\alpha} \tag{4}$$

where Q is a geometry factor of order unity, σ is the applied stress and α is the initial crack length. Clearly, as the stress level σ increases, the value of K_I is increased. As there is a greater mismatch between carbides and the ferrite, the stress level at the carbides is usually higher than that at grain boundaries and subgrain boundaries (Fig. 5). Therefore, based on Eq. (4), during the tensile process, as the applied stress increases, the stress intensity factor near the $M_{23}C_6$ carbides will first exceed the critical fracture toughness K_C, so cracks will first initiate near the $M_{23}C_6$ carbides (Fig. 10b). After crack initiation, as the stretching process continues, the stress level at the grain boundary is significantly higher than that within the grain, resulting in a higher stress intensity in the grain boundary direction than in the grain direction. Therefore, the propagation rate of the crack in the grain boundary direction is also significantly higher than

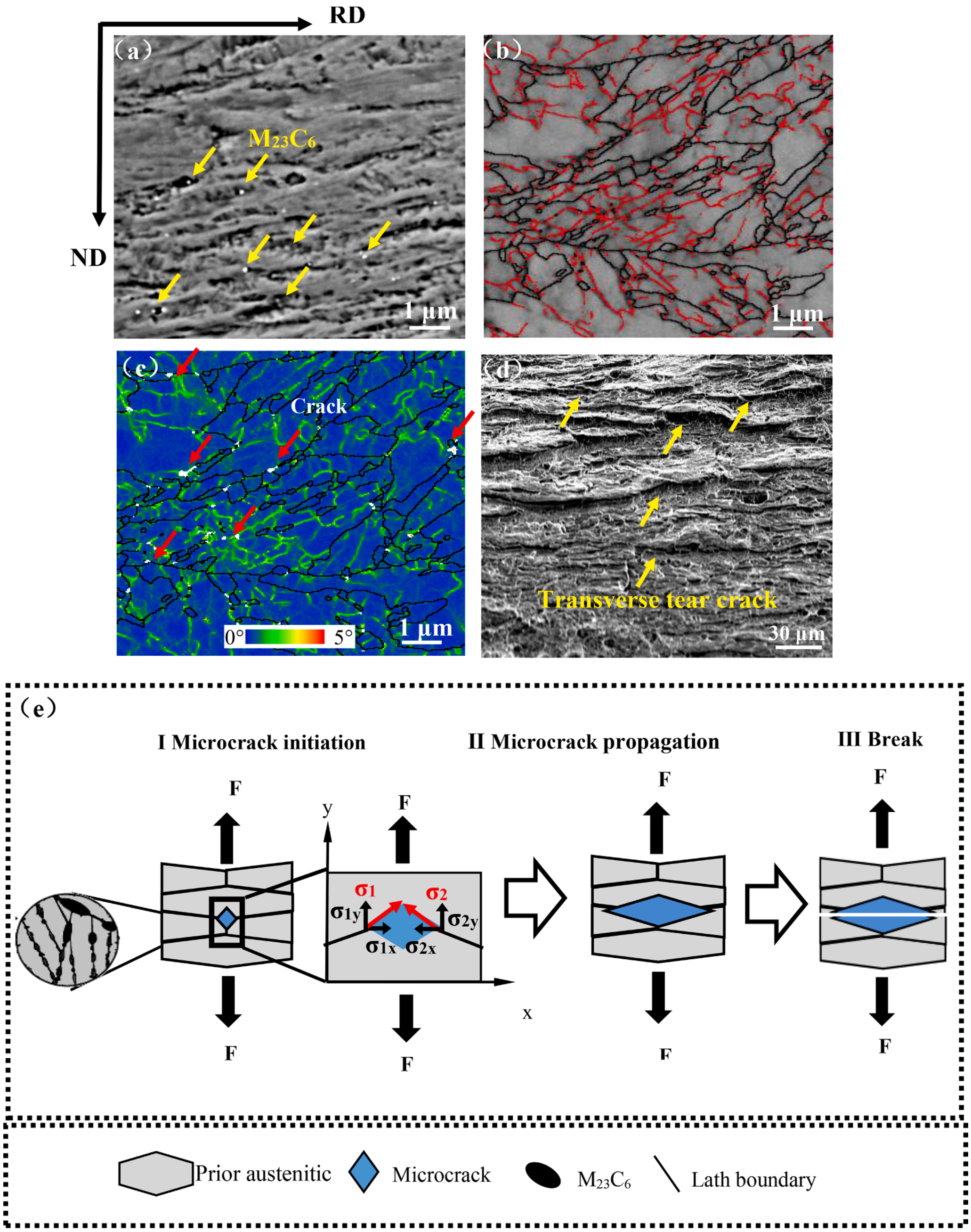

Fig. 13. Room temperature mechanisms for the CLAM steel in the normal direction. (a) Scanning electron microscopy images showing crack initiation and propagation. (b) Band contrast and grain-boundary maps near the fracture surface obtained from electron backscatter diffraction (EBSD). (c) A map of the kernel average misorientation (KAM) derived from EBSD data in {100}, {111}, and {110} orientations to illustrate the local misorientation across the grains. (d) Morphology of the steel tensile fracture surface. (e) Schematic diagram for the room temperature ductility mechanisms.

that within the grain, ultimately leading to longitudinal tearing along the layered grain boundary (Fig. 10a).

Subsequently, as the cracks continue to expand, the pattern gradually forms definitive necking under the action of the horizontal compressive stress, with the initiation and extension of new microcracks occurring at the grain boundaries under the action of the tensile stress. The dual effect of new microcrack formation and necking serves to significantly reduce the cross-sectional area, thereby rapidly increasing the actual tensile stress on the matrix. When the external stress exceeds the capacity of the ferrite laths, they will instantly tear apart. It should be noted that the expansion of the primary microcracks also consumes a significant amount of energy which effectively increases the efficiency of energy release to further suppress the initiation and expansion of subsequent microcracks. Therefore, aside from the evident tear fractures, the size of the remaining voids are comparatively small (Fig. 12aIII). This corresponds to the significant longitudinal tears and sparse fine microvoids on the fracture morphology (Fig. 11a and b).

In addition, the expansion of the longitudinal microcracks increases their boundary length significantly. A major reason for the necking is the transverse compressive stress acting on the microcrack boundaries; the longitudinal extension of these microcracks substantially increases the deformation region of the necking, as shown in Fig. 12c. The promotion of the neck obviously causes a decrease in the specimen cross-sectional area which in turn elevates the actual tensile stress in this region; therefore, the longitudinal microcrack extension serves to the increase of the necking region area, thereby enhancing the ductility of the steel.

4.3. ND room temperature ductility mechanisms

Similar to the rolling direction (RD), due to the large mismatch between the carbides and the ferrite, microcracks also initiated at the carbide/ferrite interfaces (Fig. 13a). Once the microcracks form, they also tend to propagate along the grain boundaries, due to the high stress concentration and high mismatch between the carbide/grain boundaries interfaces. This is shown in Fig. 13b and c by the band contrast and grain boundary and kernel average misorientation maps near the fracture surface obtained from electron backscatter diffraction (EBSD) analysis. However, as the direction of the layered grain boundary is perpendicular to the direction of applied stress in the ND specimens (which is parallel to the layered grain boundary in RD specimens), the fracture morphology of the steel is significantly different from the RD pattern, with many transverse tears appearing instead of longitudinal tears (Fig. 13d). The transverse tearing in the fracture surface is also the main reason for the significant decrease in elongation of the ND specimens.

Fig. 13e shows a schematic diagram of the tensile microcrack propagation at room temperature in the ND lamellar CLAM steel. Similar to the RD sample, when cracks initiate near the $M_{23}C_6$ carbides under the action of external stress, they still propagate laterally under the longitudinal tensile stresses σ_{1y} and $\sigma_{2y,}$ and propagate longitudinally under the transverse compressive stresses σ_{1x} and $\sigma_{2x.}$ However, unlike RD samples, the layered grain boundaries are perpendicular to the direction of applied stress (Fig. 13eI). Under the action of the longitudinal tensile stress, microcracks are more likely to propagate laterally along the layered grains due to the large degree of mismatch at the grain boundaries. The degree of mismatch of the smaller ferrite grains inhibits the longitudinal propagation of cracks, resulting in their transverse propagation (Fig. 13eII), corresponding to the transverse tears in Fig. 12d. Afterwards, as the transverse cracks continue to expand, the structure will fracture when the applied stress exceeds the capacity of the ferrite (Fig. 13eIII). It should be noted that the promotion of transverse cracking will accelerate the fracture of the material, while the suppression of longitudinal cracking will reduce the necking area (corresponding to the necking area in Fig. 7b), thereby reducing the ductility of the material.

4.4. High-temperature strength mechanisms

The high-temperature strengthening of the lamellar CLAM steel also results from higher subgrain and precipitation strengthening (Jin et al., 2018; Zheng et al., 2023). Under elevated temperature conditions, the strength of the grain boundaries will significantly decrease (Zhang et al., 2022; Jiao et al., 2019); accordingly for metallic materials, the decrease in high-temperature strength is often a consequence of relative sliding between the grains. Although the grain size of the lamellar CLAM steel is extremely small, subgrain strengthening and precipitation strengthening can generate more external stress to be tolerated by the grains, which markedly reduces

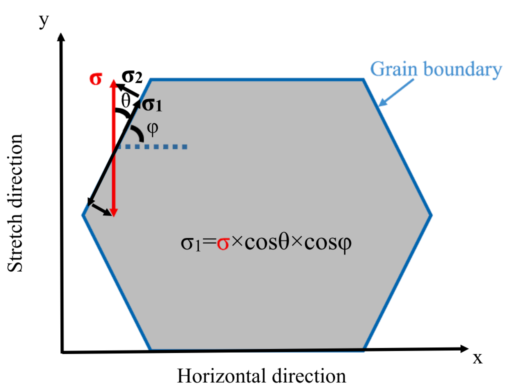

Fig. 14. Schematic diagram for the grain boundaries relative sliding force analysis.

the stress directly acting on the grain boundaries. Moreover, due to the lack of transverse grain boundaries in the layered CLAM steel, the grain boundaries are mostly parallel to the direction of external forces, making it difficult for external forces to directly act on the grain boundaries. Fig. 14 shows a schematic diagram of the relative sliding force analysis of the grain boundaries. Clearly, decomposing the tensile stress σ in the grain boundary direction and perpendicular to the grain boundary direction can induce the σ_1 and σ_2 stresses, in which the σ_1 stress can cause relative sliding of the boundaries. The relationship between σ_1 and σ conforms to the Schmidt factor calculation formula; this can be calculated using Eq. (5) (Xia et al., 2019):

$$\sigma_1 = \sigma\cos\theta\cos\varphi, \tag{5}$$

where θ is the angle between the grain boundary and the stretch direction, and φ is the angle between the grain boundary and the horizontal direction. As $\theta + \varphi = 90^\circ$, when $\theta = \varphi = 45^\circ$, σ_1 reaches its maximum value; as θ or φ continue to increase or decrease, σ_1 is continuously reduced. When $\theta = \varphi = 45^\circ$, the grains are approximately equiaxed, while in the layered grains obtained in this experiment, the θ is significantly greater than 45° and φ is significantly less than 45° for the rolling direction, while for the normal direction φ is significantly greater than 45° and θ is significantly less than 45° (Fig. 2). Therefore, in layered grains, when the applied stress is the same, the stress used to promote relative slip between grain boundaries is much smaller than that with equiaxed grains. Consequently, compared to equiaxed grains, the intergranular microcrack formation of layered grain boundaries requires greater external forces. In this regard, the layered structured CLAM steel is similar to that of a columnar-grained superalloy, where the columnar grains can also improve high-temperature strength compared to that in equiaxed-grained superalloys (Murr et al., 2013). However, compared to the directional solidification process used for preparing columnar grains in such alloys, the rolling and tempering process used in this experiment for the layered structured CLAM steel is far simpler and thus easier to commercialize.

4.5. RD high-temperature ductility mechanisms

With respect to the high-temperature ductility mechanism of the RD lamellar CLAM steel, the markedly lower grain boundary strength at high temperatures becomes considerably lower than the strength of the grains, such that no detectable longitudinal tears, *i.e.*, delamination cracks, are observed (Fig. 15a). Fig. 14b shows the morphology of the initiation and propagation of microcracks in this steel. Distinct from room temperature conditions, under high temperature stretching, the initiation and propagation of microcracks were only observed near the grain boundaries. Observations of the band contrast and the grain boundary and KAM maps near the fracture surface obtained from EBSD analysis indicated that microcracks also initiate from grain boundaries and then longitudinally extend along the lamellar grain boundaries at high temperatures (Fig. 15c and d). The only difference between the high temperature

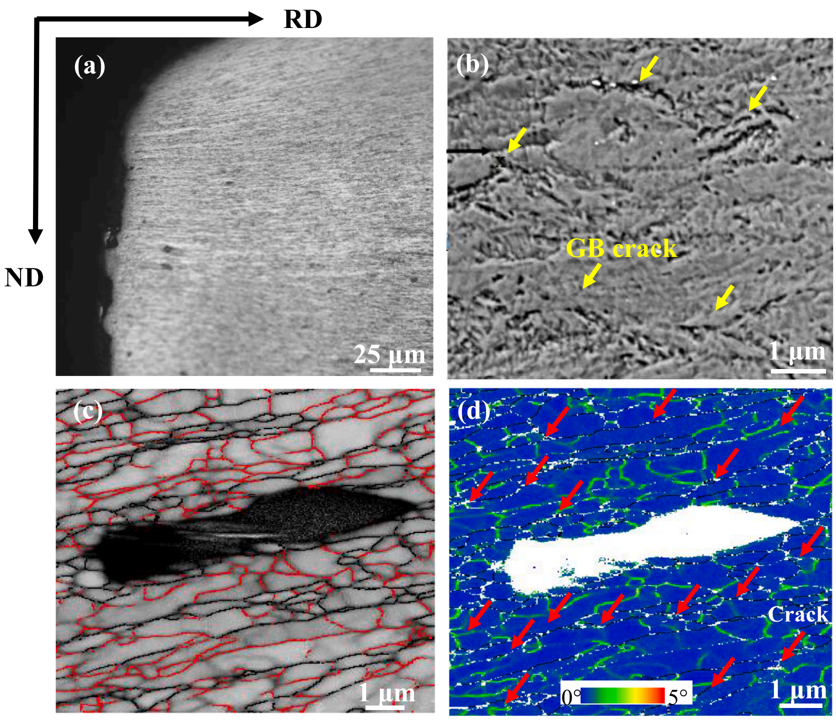

Fig. 15. 600 °C ductility mechanisms for the CLAM steel in rolling direction. (a) Optimal microscopy images of the through-thickness section normal to the 600 °C fracture surface. (b) Scanning electron microscopy images showing the crack initiation and propagation. (c) Band contrast and grain-boundary maps near the fracture surface obtained from electron backscatter diffraction (EBSD). (d) A map of the kernel average misorientation (KAM) derived from EBSD data in {100}, {111}, and {110} orientations to illustrate the local misorientation across the grains.

and room temperature stretching is that the location of the microcrack initiation and propagation at the grain boundaries (the white area depicted by the red arrows in Fig. 15d) is greatly increased, which indicates that severe deformation has occurred at the grain boundaries. Fig. 16a and b shows the high-temperature tensile fracture morphology of the RD steel with numerous fine dimples distributed with an average size of ~0.5 μm, while the size of high-temperature tensile fracture dimples in traditional CLAM steels are usually larger than 3 μm (Jin et al., 2018; Xue et al., 2019). The smaller size of the dimples in the current steel indicates that the lateral propagation of microcracks is largely suppressed.

A schematic diagram of the high-temperature tensile fracture process of the RD lamellar CLAM steel is shown in Fig. 17. Due to the high degree of distortion in the atomic arrangement at the grain boundaries, atoms in the boundaries have a stronger diffusional driving force at high temperatures to return to their equilibrium positions. Therefore, the strength of the grain boundaries will be significantly weakened. The consequent weakening of the grain boundary strength under high-temperature tension conditions will promote relative sliding between the grain boundaries (Fig. 17aI). At the same time, the relative sliding of the grain boundaries also promotes the initiation and propagation of microcracks near them due to the high degree of mismatch between the atoms at the grain boundaries and inside the grains (Fig. 17aII) which corresponds to the large number of microcracks near the grain boundaries (Fig. 14d). Similar to room temperature, due to the small degree of distortion in the grains, it is difficult for the microcracks to propagate into the grain under the applied stress, so they will preferentially expand longitudinally along the grain boundaries. This process corresponds to a plane-strain crack propagation process. Due to the relative sliding of grain boundaries, significant stress concentration occurs at the grain boundaries. According to Eq. (4), the stress concentration at the grain boundaries significantly increases the stress intensity factor near these boundaries, thereby prioritizing the initiation of cracks there. Subsequently, as the stretching process continues, the stress level at the grain boundary remains higher than that of the grain, such that the rate of crack propagation along the grain boundary is consistently higher than that within the grain. Ultimately, the cracks continue to propagate along the layered grain boundaries.

After that, with the increase in applied stress, the number of longitudinal microcracks will continue to increase under the dual action of relative sliding of grain boundaries and longitudinal crack propagation. This increase in the longitudinal cracks also markedly raises the necking area of the steel, thereby significantly increasing its degree of ductility (Fig. 17b). Similarly with the increase of cracks and the continuation of the necking process, when the external stress exceeds the capacity of ferrite laths, the material will fracture (Fig. 17aIII). The occurrence of multiple crack initiations and the slower transverse expansion rate of the cracks is reflected by the fine dispersed dimples on the fracture surface (Fig. 16a and b).

4.6. ND high-temperature ductility mechanisms

Consistent with the rolling direction, cracks still preferentially initiate near grain boundaries during the high temperature stretching process of normal direction (ND) specimens (Fig. 18a). The band contrast and the grain boundary and KAM maps near the fracture surface obtained from EBSD analysis also indicate that a large number of microcracks form at the grain boundaries. The only difference between RD and ND samples is that in the ND specimens the applied stress is perpendicular to the layered grain boundary, which promotes the transverse propagation of cracks; this makes the fracture surface of the ND specimens significantly different from that of the RD specimens. Fig. 18d shows the fracture morphology of an ND specimen, illustrating the presence of a large number of elliptical dimples in the fracture surface. This indicates that the lateral propagation rate of dimples during stretching is significantly higher than in other directions.

A schematic diagram of the high-temperature tensile fracture process of the ND lamellar CLAM steel is shown in Fig. 18e. Similar to the rolling direction, under high temperature conditions, relative sliding at grain boundaries is likely to occur due to the weakening of

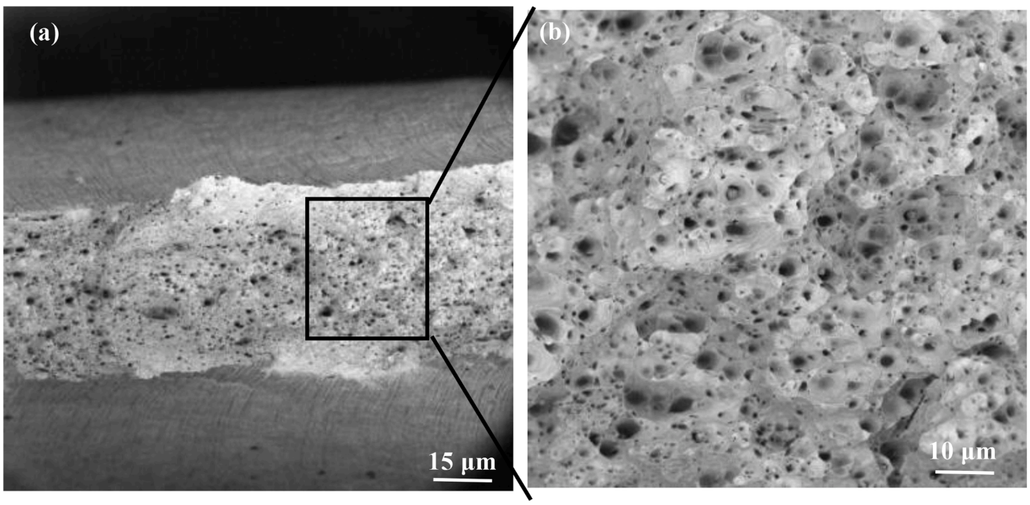

Fig. 16. Morphology of the 600 °C tensile fracture surface (a, b) in the rolling direction.

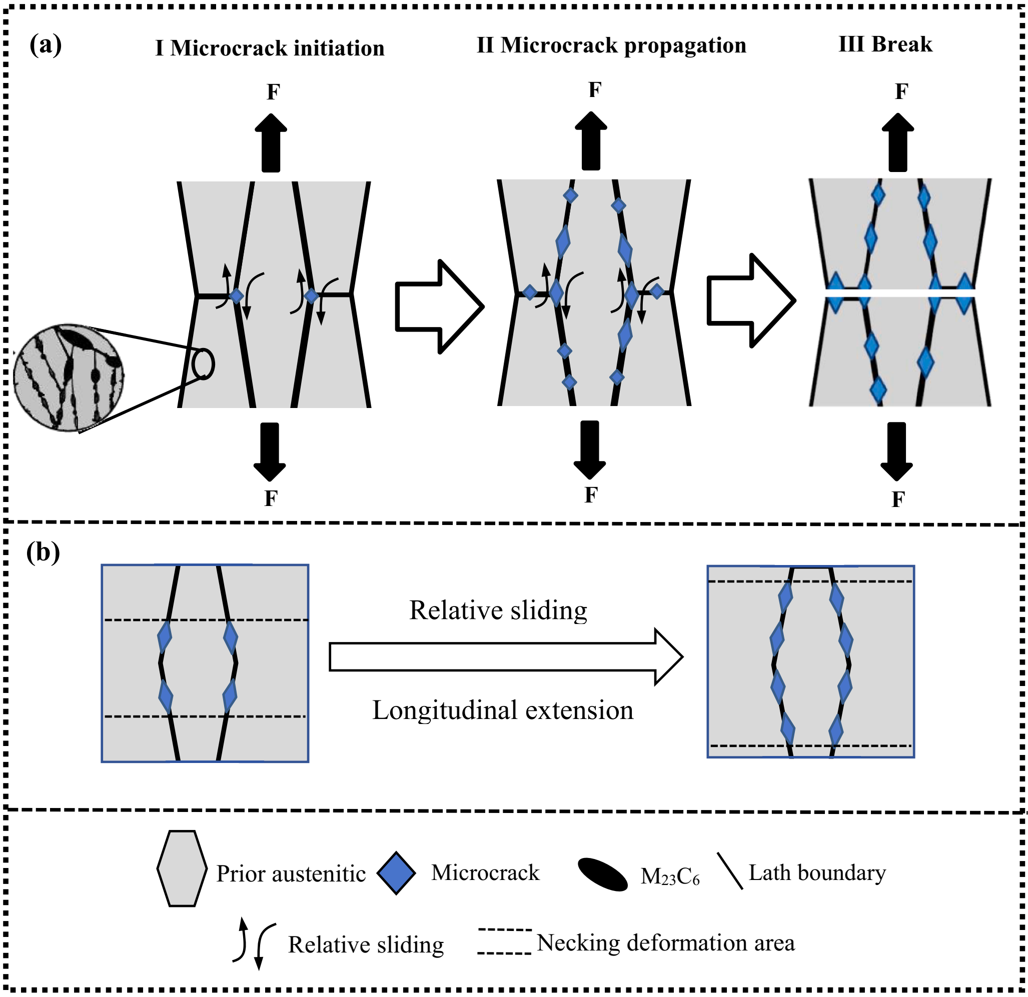

Fig. 17. Schematic diagram for the high temperature ductility mechanisms in the rolling direction. (a) Tensile crack propagation in the lamellar CLAM steel; (b and c) the propagation of a crack under tensile conditions.

grain boundaries; the relative sliding of the grain boundaries thus promotes the initiation of grain boundary cracks (Fig 18eI). Due to the large degree of mismatch at these boundaries, cracks are more likely to propagate along transverse grain boundaries under external stress (Fig 18eII) which corresponds to the elliptical dimples in Fig. 16d. Subsequently, as the cracks continue to expand, the sample will fracture when the applied stress exceeds the capacity of the ferrite (Fig. 18eIII). The lateral propagation of cracks also reduces the necking area of the steel, resulting in a significant decrease in the elongation of the steel.

5. Ductility mechanisms in the RD lamellar grain structure steel

The large degree of atomic mismatch usually makes cracks propagate from the grain boundaries. Due to the fewer transverse grain boundaries, RD layered structural materials exhibit completely different ductility mechanisms compared to the equiaxed structural materials. For RD laminated structures, due to the lack of transverse grain boundaries, the lateral expansion of cracks is significantly hindered, such that they tend to propagate longitudinally along the laminar grain boundaries. The longitudinal expansion of cracks also significantly increases the necking area in the material, thereby increasing its tensile ductility. With the change in the strength between the grain boundaries and grains, the longitudinal propagation pattern of cracks also varies. When the strength of the grain boundaries exceeds that of the grains, cracks will continuously expand along the layered grain boundaries, eventually resulting in macroscopically visible delamination fracture. When the strength of the grains exceeds that of the grain boundaries, cracks will continuously form through the relative sliding of the grain boundaries, so that a large number of small cracks will initiate and propagate longitudinally along the layered boundaries. Depending on the relative strength of the grain boundaries and grains, a transition between two different crack propagation mechanisms is apparent, as shown in Fig. 19.

Due to the propagation of cracks being often caused by stress concentration, the longitudinal propagation of cracks in layered structures must correspond to the longitudinal distribution of stress. Therefore, for lamellar TRIP steels (Li et al., 2023; Liu et al.,

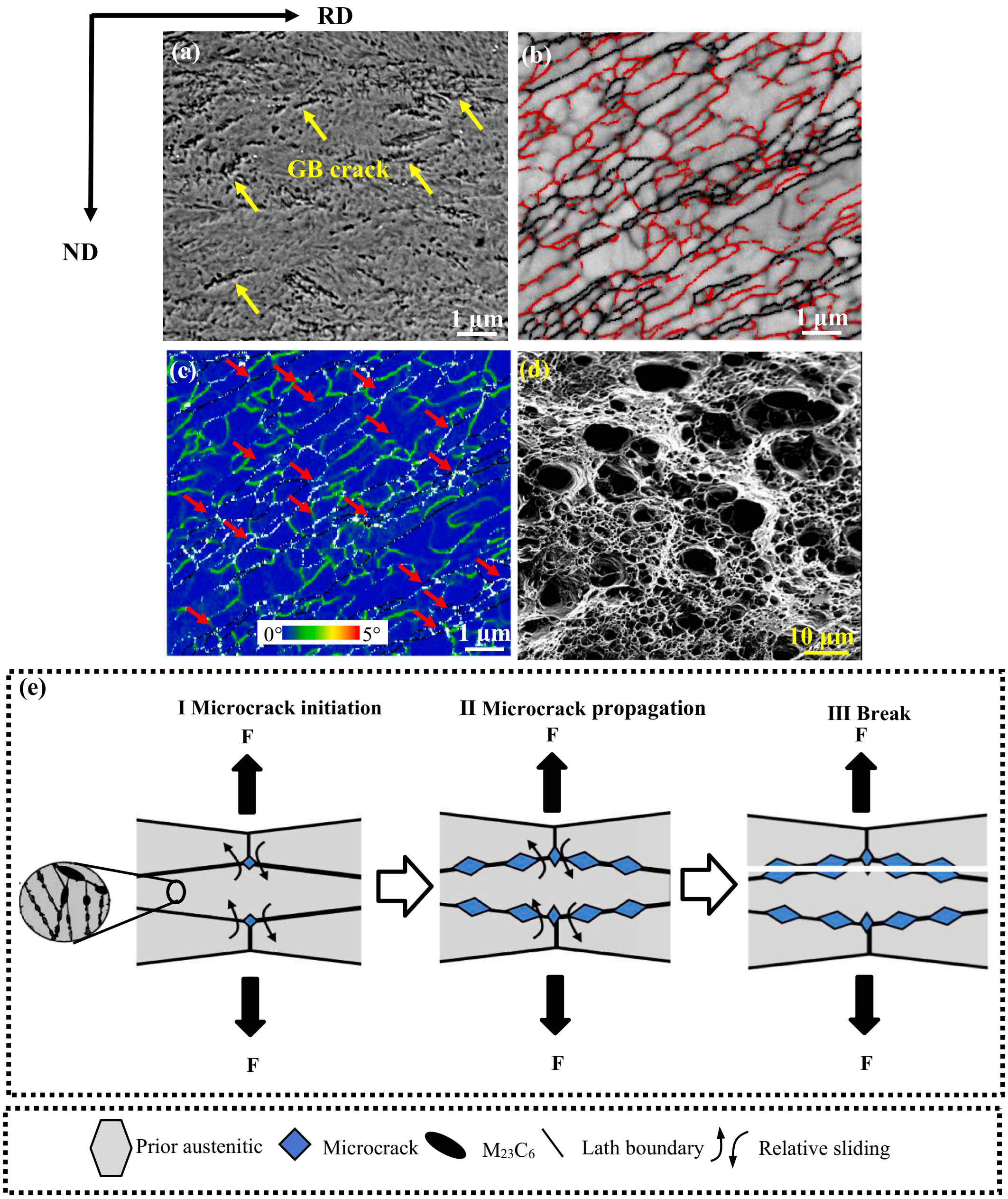

Fig. 18. Mechanisms for the CLAM steel at 600 ℃ in the normal direction. (a) Band contrast and grain-boundary maps near the fracture surface obtained from electron backscatter diffraction (EBSD). (b) A map of the kernel average misorientation (KAM) derived from EBSD data in {100}, {111}, and {110} orientations to illustrate the local misorientation across the grains. (**c**) Scanning electron microscopy images showing the crack initiation and propagation. (d) Morphology of the tensile fracture surface. (e) Schematic diagram for the room temperature ductility mechanisms.

2020), one of the reasons for their excellent ductility should be that the stress distributed along the longitudinal direction enables more areas to undergo TRIP effects. The research of Li et al. (2023) also showed that the layered structure increases the austenite conversion rate in TRIP steel from 35 % to nearly 100 %.

At present, the enhancement of material ductility is typically accomplished by reducing the hindrance of the microstructure to dislocation mobility, which invariably results in a decrease in strength. However, the improvement of material ductility through a lamellar structure is achieved by altering the mode of stress and crack propagation, thereby enabling more regions to participate in plastic deformation with less impact on strength. Therefore the combination of the lamellar structure with existing strengthening mechanisms can effectively improve the materials tensile properties. For example, the combination of a lamellar structure in a TRIP steel can result strengths exceeding than 2 GPa with excellent elongation (Li et al., 2023; Liu et al., 2020). In this work, the combination of a lamellar structure and interface and precipitation strengthening in a ferrite steel can also enhance strength by 30 % without any

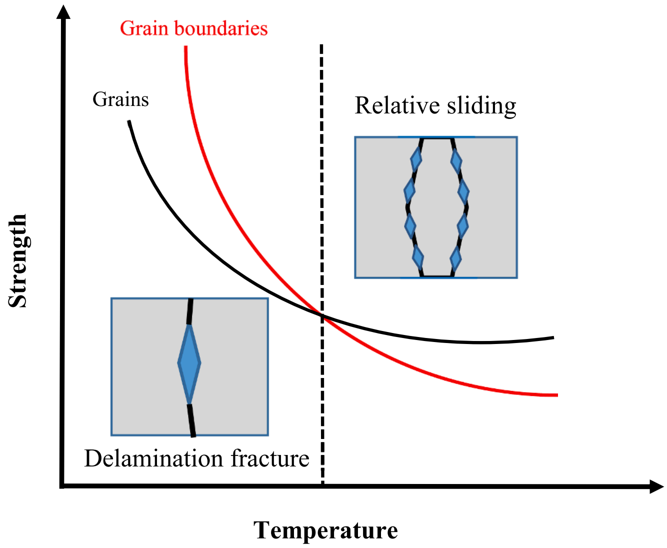

Fig. 19. Schematic illustration of the ductility mechanisms of the lamellar grain structure steel in the rolling direction.

loss in elongation.

6. Summary

In this work, we prepared a CLAM steel with a layered structure, which displays excellent tensile properties in the rolling direction and exhibits a unique plasticity mechanism. The main conclusions can be described as follows:

(1) The room temperature yield strength of the layered CLAM steel along the rolling direction is 900 ± 10 MPa, with a maximum elongation of 18 ± 1 %; these values are respectively 480 ± 10 MPa and 20 ± 1 % at 600 °C. Compared with an equiaxed grain CLAM steel, the layered structure enhances its strength by 25 % without loss of elongation at both room temperature and 600 °C.
(2) The increase in strength of the layered CLAM steel at room temperature and 600 °C is mainly due to the refinement of the size of the subgrains and $M_{23}C_6$ carbides.
(3) At room temperature, the improvement in ductility of the RD layered CLAM steel is mainly due to the large mismatch between grain boundaries and intergranular boundaries, which causes cracks to continuously propagate along grain boundaries and ultimately form longitudinal tears, leading to an increase in the necking area of the steel and reduce the local stress concentration.
(4) At 600 °C, the increase in plasticity of the RD layered CLAM steel is due to the weakening of the grain boundaries, which leads to relative sliding of these boundaries, resulting in a series of small cracks along the layered grain boundaries. These cracks serve to enhance the necking area of the steel and reduce the local stress concentration.

We believe that these results can provide a basis for further improvements in the matching of the strength and ductility in metallic alloys at ambient to high temperatures, particularly for the steels that have potential application in nuclear fusion reactors.

Funding

This project was supported by the Natural Science Foundation of China (NSFC) under grant No. 62001312.

CRediT authorship contribution statement

J.H. Zhou: Data curation, Writing – original draft. **J. Wang:** Methodology. **Robert O. Ritchie:** Writing – original draft. **Y.C. Wu:** . **J.W. Cheng:** Methodology. **L. Wang:** Supervision. **X.W. Yin:** Methodology, Supervision. **Y.F. Jiang:** Formal analysis. **J.G. Ren:** Formal analysis.

Declaration of Competing Interest

The authors declare that they have no known competing financial interests or personal relationships that could have appeared to influence the work reported in this paper.

Data availability

Data will be made available on request.

References

Abe, F., Araki, H., Noda, T., 1991. The effect of tungsten on dislocation recovery and precipitation behavior of low-activation martensitic 9Cr steels. Metall. Trans. A 22, 2225–2235.

Bloom, E.E., Conn, R.W., Davis, J.W., Gold, R.E., Little, R., Schultz, K.R., Smith, D.L., Wiffen, F.W., 1984. Low activation materials for fusion applications. J. Nucl. Mater. 122, 17–26.

Chandan, A.K., Kishore, K., Hung, P.T., Ghosh, M., Chowdhury, S.G., Kawasaki, M., Gubicza, J., 2022. Effect of nickel addition on enhancing nano-structuring and suppressing TRIP effect in $Fe_{40}Mn_{40}Co_{10}Cr_{10}$ high entropy alloy during high-pressure torsion. Int. J. Plast. 150, 103193.

Chen, S.Y., Qiao, J.B., Diao, H.Y., Yang, T.F., Poplawsky, J., Li, M.W.D.F.C., Tong, Y., Jiang, L., Liaw, P.K., Gao, Y.F., 2023. Extraordinary creep resistance in a non-equiatomic high-entropy alloy from the optimum solid-solution strengthening and stress-assisted precipitation process. Acta Mater. 244, 118600.

Chen, S.H., Jin, X.J., Rong, L.J., 2015. Improving the strength and ductility of reduced activation ferritic/martensitic steel by cold-swaging and post-annealing. Mater. Sci. Eng. A 631, 139–143.

Cho, K.S., Park, S.S., Choi, D.H., Kwon, H., 2015. Influence of Ti addition on the microstructure and mechanical properties of a 5% Cr-Mo-V steel. J. Alloy. Compd. 626, 314–322.

Dethloff, C., Gaganidze, E., Aktaa, J., 2014. Quantitative TEM analysis of precipitation and grain boundary segregation in neutron irradiated EUROFER97. J. Nucl. Mater. 454, 323–331.

Fang, Q.H., Huang, Z., Li, L., Huang, Z.W., Liu, B., Liu, Y., Li, J., Liaw, P.K., 2022. Modeling the competition between solid solution and precipitate strengthening of alloys in a 3D space. Int. J. Plast. 149, 103152.

George, E.P., Raabe, D., Ritchie, R.O., 2019. High-entropy alloys. Nat. Rev. Mater. 4, 515–534.

He, Z.F., Jia, N., Yan, H.L., Shen, Y.F., Zhu, M.W., Guan, X.J., Zhao, X.L., Jin, S.B., Sha, G., Zhu, Y.T., Liu, C.T., 2021. Multi-heterostructure and mechanical properties of N-doped FeMnCoCr high entropy alloy. Int. J. Plast. 139, 102965.

Irwin, G.R., 1957. Analysis of stresses and strains near the end of a crack traversing a plate 1957. J. Appl. Mech. 24, 361–364.

Jin, X.J., Chen, S.H., Rong, L.J., 2018. Microstructure modification and mechanical property improvement of reduced activation ferritic/martensitic steel by severe plastic deformation. Mater. Sci. Eng. A 712, 97–107.

Jiao, Y., Huang, L.J., Wei, S.L., Peng, H.X., An, Q., Jiang, S., Geng, L., 2019. Constructing two-scale network microstructure with nano-Ti5Si3 for superhigh creep resistance. J. Mater. Sci. Technol. 35, 1532–1542.

Klueh, R.L., Cheng, E.T., Grossbeck, M.L., Bloom, E.E., 2000. Impurity effects on reduced-activation ferritic steels developed for fusion applications. J. Nucl. Mater. 280, 353–359.

Klueh, R.L., Shingledecker, J.P., Swindeman, R.W., Hoelzer, D.T., 2005. Oxide dispersion - strengthened steels, a comparison of some commercial and experimental alloys. J. Nucl. Mater. 341, 103–114.

Lai, Q.Q., Yang, H.Q., Wei, Y.T., Zhou, H., Xiao, L.R., Ying, H.Q., Lan, S., You, Z.S., Kou, Z.D., Feng, T., Lu, Q., Jacques, P., Pardoen, T., 2022. Transformation plasticity in high strength, ductile ultrafine-grained FeMn alloy processed by heavy ausforming. Int. J. Plast. 148, 103151.

Li, X., Lu, K., 2017. Playing with defects in metals. Nat. Mater. 16, 700–701.

Li, Y.J., Yuan, G., Li, L.L., Kang, J., Yan, F.K., Du, P.J., Raabe, D., Wang, G.D., 2023a. Ductile 2-GPa steels with hierarchical substructure. Science 379, 168–173.

Li, Y.Z., Liang, Z.Y., Huang, M.X., 2022. Strengthening contributions of dislocations and twins in warm-rolled TWIP steels. Int. J. Plast. 150, 103198.

Li, K.S., Wang, R.Z., Zhang, X.C., Tu, S.T., 2023b. Creep-fatigue damage mechanisms and life prediction based on crystal plasticity combined with grain boundary cavity model in a nickel-based superalloy at 650℃. Int. J. Plast. 165, 103601.

Liu, L., Yu, Q., Wang, Z., Ell, J., Huang, M.X., Ritchie, R.O., 2020. Making ultrastrong steel tough by grain-boundary delamination. Science 368, 1347–1352.

Li, Y.F., Nagasaka, T., Muroga, T., Kimura, A., Ukai, S., 2011. High-temperature mechanical properties and microstructure of 9Cr oxide dispersion strengthened steel compared with RAFMs. Fusion Eng. Des. 86, 2495–2499.

Li, Y.Z., Zhao, S.L., He, S.H., Huang, C.P., Huang, M.X., 2022b. Enhancing yield stress and uniform elongation in an ultrathin packaging steel via controlling dislocation density. Int. J. Plast. 155, 103334.

Li, Y., Huang, Q., Wu, Y., Nagasaka, T., Muroga, T., 2007. Mechanical properties and microstructures of China low activation martensitic steel compared with JLF-1. J. Nucl. Mater. 367-370, 117–121.

Liu, G.L., Yang, S.W., Ding, J.W., Han, W.T., Zhou, L.J., Zhang, M.Q., Zhou, S.S., Misra, R.D.K., Wan, F.R., Shang, C.J., 2019. Formation and evolution of layered structure in dissimilar welded joints between ferritic-martensitic steel and 316L stainless steel with fillers. J. Mater. Sci. Technol. 35, 2665–2681.

Lucas, G.E., 1993. The evolution of mechanical property change in irradiated austenitic stainless steels. J. Nucl. Mater. 206, 287–305.

Murr, L.E., Martinez, E., Pan, X.M., Gaytan, S.M., Castro, J.A., Terrazas, C.A., Medina, F., Wicker, R.B., Abbott, D.H., 2013. Microstructures of Rene 142 nickel-based superalloy fabricated by electron beam melting. Acta Mater. 61, 4289–4296.

Noda, T., Abe, F., Araki, H., Okada, M., 1988. Materials selection for reduced activation of fusion reactors. J. Nucl. Mater. 155-157, 581–584.

Noh, S., Ando, M., Tanigawa, H., Fujii, H., Kimura, A., 2016. Friction stir welding of F82H steel for fusion applications. J. Nucl. Mater. 478, 1–6.

Peng, Z.F., Liu, S., Yang, C., Chen, F.Y., Peng, F.F., 2018. The effect of phase parameter variation on hardness of P91 components after service exposures at 530–550°C. Acta Mater. 143, 141–155.

Petch, N.J., 1953. The cleavage strength of polycrystals. J. Iron Steel Inst. Jpn. 174, 25–28.

Ritchie, R.O., 2011. The conflicts between strength and toughness. Nat. Mater. 10, 817–822.

Sasaki, T.T., Oh-ishi, K., Ohkubo, T., Hono, K., 2011. Effect of double aging and microalloying on the age hardening behavior of a Mg-Sn-Zn alloy. Mater. Sci. Eng. A 530, 1–8.

Shi, Y.N., Lu, Z., Xu, H.J., Xie, R., Ren, Y.H., Yang, G., 2019. Microstructure characterization and mechanical properties of laser additive manufactured oxide dispersion strengthened Fe-9Cr alloy. J. Alloy. Compd. 791, 121–133.

Tan, L., Snead, L.L., Katoh, Y., 2016. Development of new generation reduced activation ferritic martensitic steels for advanced fusion reactors. J. Nucl. Mater. 478, 42–49.

Tang, W.S., Yang, X.Q., Li, S.L., Li, H.J., 2019. Microstructure and properties of CLAM/316L steel friction stir welded joints. J. Mater. Process. Tech. 271, 189–201.

Tian, S.G., Zhang, B.S., Yu, H.C., Tian, N., Li, Q.Y., 2016. Micro structure evolution and creep behaviors of a directionally solidified nickel-base alloy under long-life service condition. Mater. Sci. Eng. A 673, 391–399.

Tiamiyu, A.A., Tari, V., Szpunar, J.A., Odeshi, A.G., Khan, A.K., 2018. Effects of grain refinement on the quasi-static compressive behavior of AISI 321 austenitic stainless steel: EBSD, TEM, and XRD studies. Int. J. Plast. 107, 79–99.

Wang, J., Lu, S.P., Rong, L.J., Li, D.Z., 2015. Thermal cycling, microstructure and mechanical properties of 9Cr2WVTa steel welds. J. Mater. Process. Technol. 222, 434–443.

Wang, Z., Huang, M.X., 2020. Optimising the strength-ductility-toughness combination in ultra-high strength quenching and partitioning steels by tailoring martensite matrix and retained austenite. Int. J. Plast. 134, 102851.

Wang, L., Yao, C.L., Shen, J., Zhang, Y.P., Liu, G., Wu, X.Y., Zhang, G.J., 2022. A new method to design eutectic high-entropy alloys by determining the formation of single-phase solid solution and calculating solidification paths. Mater. Sci. Eng. A 830, 142325.

Wang, W., Xu, G., Song, L.L., 2019. Long-term stability of precipitated phases in CLAM steel during thermal aging. J. Nucl. Mater. 521, 56–62.
Xue, W.Y., Zhou, J.H., Shen, Y.F., Zhang, W.N., Liu, Z.Y., 2019. Micromechanical behavior of a fine-grained China low activation martensitic (CLAM) steel. J. Mater. Sci. Technol. 35, 1869–1876.
Xia, D.B., Chen, X., Huang, G.S., Bin, Jiang, Tang, A.T., Yang, H., Gavras, S., Huang, Y.D., Hort, N., Pan, F.S., 2019. Calculation of Schmid factor in Mg alloys: influence of stress state. Scr. Mater. 171, 31–35.
Xiao, F., Chu, K.J., Li, Z., Hou, R.H., Gao, Y.P., Sun, Q.P., Jin, X.J., 2023. Improved functional fatigue resistance of single crystalline NiTi micropillars with uniformly oriented Ti3Ni4 precipitates. Int. J. Plast. 160, 103480.
Yan, P.Y., Yu, L.M., Liu, Y.C., Liu, C.X., Li, H.J., Wu, J.F., 2018. Effects of Hf addition on the thermal stability of 16Cr-ODS steels at elevated aging temperatures. J. Alloy. Compd. 739, 368–379.
Yin, T.W., Shen, Y.F., Jia, N., Li, Y.J., Xue, W.Y., 2023. Controllable selection of martensitic variant enables concurrent enhancement of strength and ductility in a low-carbon steel. Int. J. Plast. 168, 103704.
Yu, L., Xiao, X.Z., Chen, L.R., Cheng, Y.Y., Duan, H.L., 2018. A hierarchical theoretical model for mechanical properties of lath martensitic steels. Int. J. Plast. 111, 135–151.
Zhang, B.B., Tang, Y.G., Mei, Q.S., Li, X.Y., Lu, K., 2022a. Inhibiting creep in nanograined alloys with stable grain boundary networks. Science 378, 659–663.
Zhang, J.W., Yu, L.M., Gao, Q.Z., Liu, C.X., Ma, Z.Q., Li, H.J., Liu, Y.C., Wang, H., 2022b. Tailoring the tempered microstructure of a novel martensitic heat resistant steel G115 through prior cold deformation and its effect on mechanical properties. Mater. Sci. Eng. A 841, 143015.
Zhang, Z.P., Huang, Q.S., Zhou, H.F., 2023. High-entropy alloy nanocrystals with low-angle grain boundary for superb plastic deformability and recoverability. Int. J. Plast. 167, 103679.
Zhang, S., Wang, L.Y., Zhu, G.M., Diehl, M., Maldar, A., Shang, X.Q., Zeng, X.Q., 2022c. Predicting grain boundary damage by machine learning. Int. J. Plast. 150, 103186.
Zhao, Y., Liu, S., Shi, J., Mao, X., 2018. Experimental and numerical simulation analysis on creep crack growth behavior of CLAM steel. Mater. Sci. Eng. A 735, 260–268.
Zhao, Q., Yu, L.M., Liua, Y.C., Huang, Y., Ma, Z.Q., Li, H.J., Wu, J.F., 2017. Microstructure and tensile properties of a 14Cr ODS ferritic steel. Mater. Sci. Eng. A 680, 347–350.
Zhou, J.H., Shen, Y.F., Xue, W.Y., Jia, N., 2021a. Hot-deformation induced static recrystallization and nano-MX precipitation in a low activation martensitic steel. J. Nucl. Mater. 556, 153190.
Zhou, J.H., Shen, Y.F., Jia, N., 2021b. Strengthening mechanisms of reduced activation ferritic/martensitic steels, a review. Int. J. Miner. Metall. Mater. 28, 335–348.
Zhou, J.H., Shen, Y.F., Hong, Y.Y., Xue, W.Y., Misra, R.D.K., 2020. Strengthening a fine-grained low activation martensitic steel by nanosized carbides. Mater. Sci. Eng. A 769, 138471.
Zhou, J.H., Shen, Y.F., Xue, W.Y., Jia, N., Misra, R.D.K., 2021c. Improving strength and ductility of low activation martensitic (LAM) steel by alloying with titanium and tempering. Mater. Sci. Eng. A 799, 140152.
Zheng, G.M., Tang, B., Zhao, S.K., Wang, J., Xie, Y.Z., Chen, X.F., Wang, W.Y., Liu, D., Yang, R., Li, J.S., 2023. Breaking the high-temperature strength-ductility trade-off in TiAl alloys through microstructural optimization. Int. J. Plast. 170, 103756.
Zhu, Y.T., Wu, X.L., 2023. Heterostructured materials. Prog. Mater. Sci 131, 101019.
Zinkle, S.J., Boutard, J.L., Hoelzer, D.T., Kimura, A., Lindau, R., Odette, G.R., Rieth, M., Tan, L., Tanigawa, H., 2017. Development of next generation tempered and ODS reduced activation ferritic/martensitic steels for fusion energy applications. Nucl. Fusion 57, 092055.